Hybrid Far- and Near-Field Modeling for Reconfigurable Intelligent Surface Assisted V2V Channels: A Sub-Array Partition Based Approach

Hao Jiang, *Member, IEEE*, Baiping Xiong, Hongming Zhang, *Member, IEEE*, and Ertugrul Basar, *Fellow, IEEE*

***Abstract*— Reconfigurable intelligent surface (RIS)-assisted communications has been a hot topic due to its promising advantages for future wireless networks. Existing works on RIS-assisted channel modeling have mainly focused on far-field propagation condition with planar wavefront assumption. In essence, the far-field condition does not always hold because the RIS array dimension may be comparable to the terminal distance, especially in RIS-assisted mobile networks. To this end, we propose a hybrid far- and near-field stochastic channel model for characterizing a RIS-assisted vehicle-to-vehicle (V2V) propagation environment, which takes into account both far-field and near-field propagation conditions. To achieve the balance between the modeling accuracy and complexity for the investigation of the RIS-assisted V2V propagation characteristics, we develop a sub-array partitioning scheme to dynamically divide the entire RIS array into several smaller sub-arrays, which makes planar wavefront assumption applicable for the sub-arrays. Important channel statistical properties, including spatial cross-correlation functions (CCFs), temporal auto-correlation functions (ACFs), and frequency correlation functions (FCFs), are derived and investigated. Simulation results are provided to show the performance of the proposed sub-array partition based hybrid far- and near-field modeling solution for RIS-assisted V2V channels.**

Manuscript received 8 August 2022; revised 10 January 2023; accepted 15 March 2023. Date of publication 31 March 2023; date of current version 13 November 2023. This work was supported in part by NSFC Projects under Grant 62101275 and Grant 62001056, in part by the Jiangsu NSF Project under Grant BK20200820, and in part by the Scientific and Technological Research Council of Turkey (TÜBITAK) under Grant 120E401. The associate editor coordinating the review of this article and approving it for publication was L. Dasilva. *(Hao Jiang and Baiping Xiong contributed equally to this work.) (Corresponding author: Hongming Zhang.)*

Hao Jiang is with the School of Artificial Intelligence/School of Future Technology, Nanjing University of Information Science and Technology, Nanjing 210044, China, and also with the National Mobile Communications Research Laboratory, Southeast University, Nanjing 210096, China (e-mail: jianghao@nuist.edu.cn).

Baiping Xiong is with the National Mobile Communications Research Laboratory, Frontiers Science Center for Mobile Information Communication and Security, Southeast University, Nanjing 210096, China, and also with the Pervasive Communication Research Center, Purple Mountain Laboratories, Nanjing 211111, China (e-mail: xiongbp@seu.edu.cn).

Hongming Zhang is with the School of Information and Communication Engineering, Beijing University of Posts and Telecommunications, Beijing 100876, China (e-mail: zhanghm@bupt.edu.cn).

Ertugrul Basar is with the Communications Research and Innovation Laboratory (CoreLab), Department of Electrical and Electronics Engineering, Koc University, Sariyer, 34450 Istanbul, Turkey (e-mail: ebasar@ku.edu.tr).

Color versions of one or more figures in this article are available at https://doi.org/10.1109/TWC.2023.3262063.

Digital Object Identifier 10.1109/TWC.2023.3262063

***Index Terms*— Reconfigurable intelligent surface, V2V channel modeling, hybrid far- and near-field communications, sub-array partition, propagation characteristics.**

I. Introduction

A. Background

As a promising technology for enhancing the link capacity and extending the coverage in wireless communication environments for sixth generation (6G) networks, reconfigurable intelligent surfaces (RISs) have recently received rapidly increasing attention from both academic and industry communities [1]. An RIS is comprised of a surface of electromagnetic material consisting of a large number of square metallic patches, each of which can be digitally controlled to induce an independent amplitude change and/or phase shift to the incident signal, thereby collaboratively altering the wireless channels between transmitters and receivers. Owing to the above appealing features, RISs have been studied extensively and incorporated into various wireless communication systems [2]. It is well known that a set of precise and easy-to-use channel models are critical for the performance evaluation of communication networks [3]; therefore, the investigation of RIS-assisted channel modeling has been a hot research topic in recent years.

B. Related Works

Most previous investigations devoting to the propagation characteristics of wireless channels can be categorized into measurement-based methods and simulation-based methods [4]. The former ones are able to determine the propagation paths and field strength of radio waves [5]. Although this type of wireless channel characterization is the most intuitive solution to capture wireless channel characteristics, it is too expensive and time-consuming to carry out a variety of measurement campaigns in wireless propagation environments. However, through the simulation-based methods, channel characteristics are investigated according to the electromagnetic wave propagation theory. In the existing literature, this type of channel models can be further separated into deterministic

and stochastic ones. It is noteworthy to mention that the accuracy of deterministic channel modeling method (e.g., ray-tracing) depends on the description of environmental layout including the terrain topography and the electromagnetic parameters of obstruction materials [6]. Therefore, the simulation of non-stationary channels using deterministic solutions yields considerable computational complexity, hence decreasing simulation efficiency. In stochastic modeling methods, wireless channels are developed by modeling channel fading characteristics as a stochastic process [7]. According to the geometric relationships among the transmitter, receiver, and obstacles, geometry-based stochastic models (GBSMs) have been widely used in recent years, and their suitabilities have been demonstrated for the simulation of highly dynamic vehicle-to-vehicle (V2V) communication channels [8]. Measurements in [9] have demonstrated that there is a wealth of angular information in the vertical plane, which indicates that three-dimensional (3D) channel models are more accurate than two-dimensional (2D) channel models when calculating the system performance. In light of this, the existing works have proposed a variety of 3D channel models to describe the V2V multiple-input multiple-output (MIMO) communication scenarios. For instance, the authors used semi-ellipsoid [10] and elliptic-cylinders [11], to describe obstacles in V2V MIMO communication environments. In these studies, the channel propagation characteristics in the spatial, time, and frequency domains were derived and discussed based on the geometric relationships.

Recently, RISs have gradually emerged in the design of wireless communication systems for achieving high communication quality by passive beamforming at the RIS [12]. This motivates many researchers to develop state-of-the-art channel models for describing the RIS-assisted wireless communication scenarios. For example, the authors in [13] proposed a 3D non-stationary MIMO channel model for RIS-assisted fixed-to-mobile communications, which derived the RIS reflection phases and time-varying angles and distances to characterize the channel non-stationary properties. However, in [13], the authors did not consider the impacts of the motion properties of the transceivers on the RIS-assisted channel characteristics, and therefore restricted the used of their channel model for 5G/6G high-dynamic communications. The authors in [14] proposed a 3D geometry-based channel model for describing the RIS-assisted MIMO propagation environments, which investigated the impacts of the motion time/direction/velocity of the transceivers on the channel propagation characteristics. The authors in [15] proposed a 3D wideband non-stationary channel model for RIS auxiliary aerial-to-ground communications at mmWave bands, the results of the propagation characteristics show that the RIS orientation angle as well as relative deployment location play roles in the performance of RIS-assisted communication systems, and meanwhile highlight the advantage of discrete RIS reflection phase configuration. In [16], the authors proposed a statistical 3D MIMO channel model for RIS-assisted wireless communications by modeling the RIS as a virtual cluster and RIS units as virtual scatterers. The impacts of the physical properties of RIS, such as unit number, unit size, relative location among the transmitter, RIS, and receiver, as well as RIS array configurations, on channel temporal and spatial correlation characteristics were investigated.

For the aforementioned research works on the investigations of the wireless propagation characteristics, they are mainly based on the far-field and plane wavefront assumptions. Although this solution has the ability to simplify the computational complexity of channel modeling, it will in principle not lead us to obtain the accurate results of wireless propagation characteristics in spatial, time, and frequency domains. To solve such open research problem, it is crucial to differentiate the far-field and near-field scenarios before investigating the RIS-assisted propagation characteristics [17], [18]. In reality, when the distance between a RIS and a transmit/receive antenna array is far beyond the Rayleigh distance, i.e., $2\mathcal{M}^2/\lambda$, where $\mathcal{M}$ represents the dimension of the antenna elements or RIS units and λ is the carrier wavelength, the investigation of the propagation characteristics should be based on the far-field and plane wavefront assumptions. However, when the number of antenna elements or RIS units is large, which results in the distance between a RIS and a transmit/receive antenna array being smaller than the Rayleigh distance, it is necessary to adopt the near-field and spherical wavefront assumptions to investigate the channel propagation characteristics [19], [20]. In the existing literature, such as [21], the authors proposed a scalable framework for demonstrating the feasibility for partitioning the large RIS array into several smaller subsets with specific sizes, which, however, failed to reveal the relationship between the sub-arrays and the physical properties of the communication environments, such as the propagation paths length. Furthermore, the existing works did not explain the motivations of the separating RIS array, and meanwhile the separating solution of the RIS array was also neglected. Therefore, it will bring difficulties for the researchers in the parameters choices of the sizes of the RIS sub-arrays.

It is worth mentioning that RISs require a large amount of units to compensate the very high path loss; however, the increasing of the RIS units will cause larger array dimension and hence larger Rayleigh distance of the RIS array. This results in the near-field propagation conditions, making conventional planar wavefront assumption invalid. Furthermore, owing to the motion of the transceivers, the near- and far-field propagation conditions will appear alternately in RIS-assisted V2V communication scenarios as shown in Fig. 2(a). In reality, the investigation of the RIS-assisted V2V channel characteristics based on the planner wavefront assumption will lead to relatively lower modeling complexity. In this case, it is not difficult to obtain the acceptable modeling accuracy for the far-field propagation condition, while the modeling accuracy is obviously insufficient for the near-field propagation condition. On the other hand, if we investigate the RIS-assisted V2V channel characteristics based on the spherical wavefront assumption, it is easy to obtain the high modeling accuracy, but the modeling complexity is very high for the far-field propagation condition. Consequently, this paper aims at addressing the

aforementioned issues by developing a hybrid far- and near-field channel model for RIS-assisted V2V channels based on a dynamic sub-array partitioning scheme, which achieves a well balance between the channel modeling accuracy and complexity for investigating the small-scale fading characteristics of RIS-assisted V2V communication systems.

C. Main Contributions

In this paper, we develop a hybrid far- and near-field 3D non-stationary MIMO end-to-end channel model for RIS-assisted V2V communications with blocking LoS path, based on a dynamic sub-array partitioning scheme. The main contributions are summarized as follows:

- We develop a 3D non-stationary MIMO end-to-end channel model for characterizing the small-scale fading characteristics of the RIS-assisted V2V communication systems, which has the ability to capture the RIS-assisted channel propagation characteristics for the far- and near-field conditions. By appropriately adjusting the model parameters, the proposed model can be adapted for various mobile communication scenarios.
- To relax the channel modeling complexity in near-field propagation condition, we propose a dynamic sub-array partitioning scheme to divide the entire RIS array into several smaller sub-arrays dynamically. In this case, we can apply planar wavefront assumption to the sub-arrays, which aims at achieving the balance between the modeling accuracy and complexity for the investigation of the small-scale fading characteristics of the RIS-assisted V2V channels. The proposed dynamic sub-array partitioning scheme is a soft-level method, which can be generalized for various mobile communication networks with large-dimension antenna arrays.
- Based on the non-isotropic scattering assumption, the statistical properties of the proposed sub-array partition based hybrid far- and near-field channel model, including the spatial cross-correlation functions (CCFs), temporal auto-correlation functions (ACFs), and frequency correlation functions (FCFs), are derived and analyzed. The results provide important guidelines for future RIS-assisted vehicular network design.
- We compare the channel modeling performances based on the proposed sub-array partitioning scheme and the traditional methods, i.e., far-field assumption (planar wavefron model), which demonstrates the advantages of the proposed hybrid far- and near-field modeling solution with high accuracy and low complexity, thereby providing a theoretical support for the design and evaluation of the RIS-assisted V2V communication systems.

The rest of this paper is organized as follows. Section II presents the system channel model, where a hybrid far- and near-field 3D non-stationary V2V channel model with the assistance of RIS is proposed. In Section III, we investigate the RIS-assisted V2V propagation characteristics based on the proposed sub-array pattern scheme. In Section IV, we provide the simulation results and discussions, and our conclusions are drawn in Section V.

Notation: The lowercase, boldface lowercase, and boldface uppercase letters such as x, $\mathbf{x}$, and $\mathbf{X}$ stand for the scalars, vectors, and matries, respectively. $\|\cdot\|$ represents the Frobenius norm and $(\cdot)^*$ is the complex conjugate operation. $[\cdot]^{\mathrm{T}}$ is the transpose operation and $\lfloor x \rceil$ takes the largest integer not greater than x. $x \sim \mathcal{CN}(\mu, \sigma^2)$ stands for a complex Gaussian variable x with mean μ and variance σ^2, and $j = \sqrt{-1}$ is the imaginary unit.

II. System Model

Let us consider a 3D geometry-based stochastic MIMO channel model for RIS-assisted V2V communications at sub-6 GHz, as shown in Fig. 1, where RIS is provided with a controller that manipulates the waves by attaching an additional reflection coefficient during the interaction [1]. The MT and MR consist of P and Q 3D positioned omni-directional uniform linear array (ULA) antennas, respectively. The global Cartesian coordinate system is established by defining the center point of the MT's antenna array as the origin, the line connecting the origin and the center of MR's antenna array as the x-axis, while z-axis is vertical upward which passes through the center of the MT array, and thus y-axis is obtained according to the right-hand rule. The spacing between two adjacent antennas at the MT and MR are denoted by δ_T and δ_R, respectively; while the orientations of the transmit and receive antenna arrays relative to the x-axis are denoted by ψ_T and ψ_R, respectively. The orientations of the transmit and receive antenna arrays relative to the azimuth plane are denoted by θ_T and θ_R, respectively. In the proposed channel model, the numbers of the columns (counting from left to right) and rows (counting from bottom to top) of the arranged units in the RIS are denoted by M and N, respectively. The sizes of each unit in the RIS along the horizontal and vertical directions are denoted by d_M and d_N, respectively.

A. Proposed Sub-Array Partitioning Scheme

Currently available RIS channel models have calculated the distance/angle parameters for all RIS units according to the geometry-based method. Although this kind of modeling solution achieves high modeling accuracy, it leads to a high computational complexity in channel modeling as the RIS requires a large amount of units to compensate the path loss [22], [23]. In the existing literature, the planar wavefront assumption has been adopted to simplify the channel modeling process in MIMO systems under far-field condition [24]. In practice, the far-field condition is not always satisfied in RIS-assisted wireless communications. This is mainly because that the dimension of RIS becomes comparable to the propagation distance and no longer negligible when the RIS units number is large; meanwhile, the terminals may move inside the near-field region of RIS, as shown in Fig. 2(a). To address this issue, we propose a sub-array partitioning scheme to divide the entire RIS array evenly into several smaller sub-arrays, where each sub-array consists of several RIS units, as shown in Fig. 2(b). For each sub-array, the far-field condition holds, meaning that the dimension of each sub-array is much smaller and negligible as compared to the propagation distances. Consequently, we

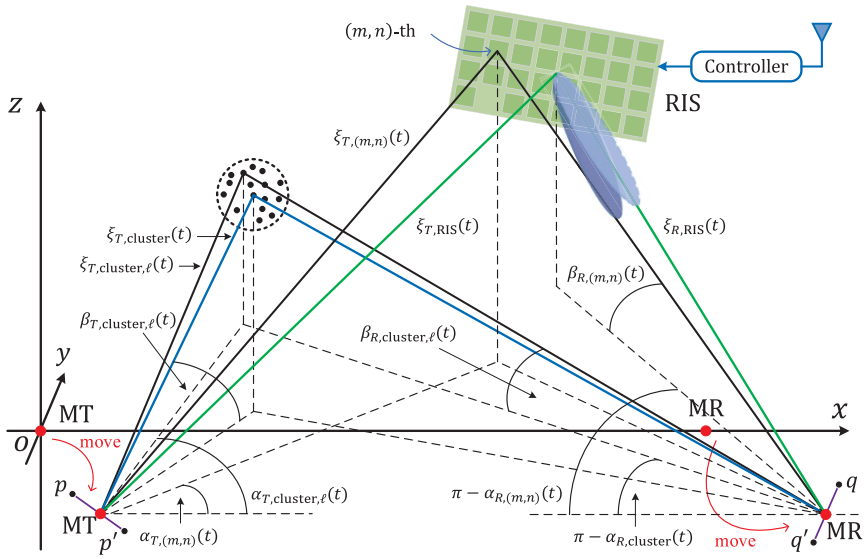

Fig. 1. Propagation paths and angular parameters of the proposed channel model.

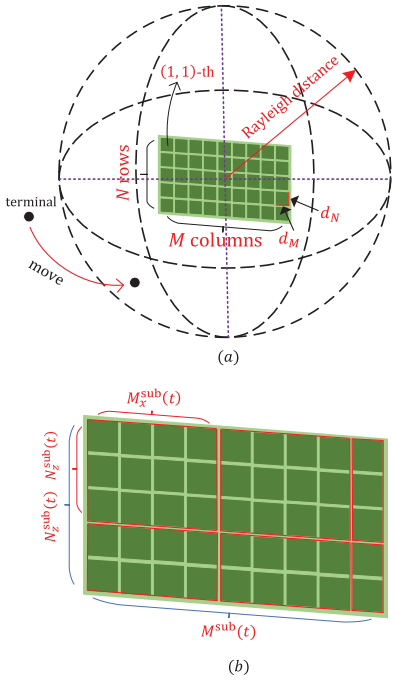

Fig. 2. Illustration of the proposed sub-array partitioning scheme.

can apply planar wavefront assumption to each sub-array. In each sub-array, once the distance/angle parameters of any one RIS unit are calculated, the distance/angle parameters of the remaining RIS units can be obtained accordingly. This significantly reduces the channel modeling complexity. In the proposed dynamic sub-array partitioning scheme, the sub-array Rayleigh distances are adopted as the boundary of far-field and near-field to perform dynamic sub-array partition, which establishes a dynamic mapping relationship between sub-arrays and physical propagation environments. As compared to the fixed partition-based model such as [21], the proposed dynamic sub-array partition-based modeling solution achieves a well balance between channel modeling accuracy and modeling complexity.

We denote t as the motion time of the MT and MR, the time-varying distance from the nearest terminal, either from the MT or MR to RIS, can be denoted by $\xi_{\text{RIS}}^{\text{ter}}(t) = \min\{\xi_{T,\text{RIS}}(t), \xi_{R,\text{RIS}}(t)\}$, where $\xi_{T,\text{RIS}}(t)$ and $\xi_{R,\text{RIS}}(t)$ represent the time-varying distances from the center positions of the MT and MR antenna arrays to that of the RIS array in the real-time motion stage, which can be respectively derived by $\xi_{T,\text{RIS}}(t) = \|\mathbf{d}_{\text{RIS}}(t) - \mathbf{d}_T(t)\|$ and $\xi_{R,\text{RIS}}(t) = \|\mathbf{d}_{\text{RIS}}(t) - \mathbf{d}_R(t)\|$. The $\mathbf{d}_{\text{RIS}} = [x_{\text{RIS}}, y_{\text{RIS}}, z_{\text{RIS}}]^{\text{T}}$ denotes the time-varying distance vector from the origin of the global coordinate system to the center point of the RIS array. The $\mathbf{d}_T(t) = [d_{T,x}(t), d_{T,y}(t), 0]^{\text{T}}$ and $\mathbf{d}_R(t) = [D_0 + d_{R,x}(t), d_{R,y}(t), 0]^{\text{T}}$ are the time-varying distance vectors from the origin of the global coordinate system to the center points of the MT and MR antenna arrays, respectively, where $d_{T,x}(t) = v_T t \cos\eta_T$, $d_{T,y}(t) = v_T t \sin\eta_T$, $d_{R,x}(t) = v_R t \cos\eta_R$, and $d_{R,y}(t) = v_R t \sin\eta_R$. The D_0 denotes the distance from the center of the MT antenna array to that of the MR antenna array. The v_T and v_R are the motion speeds of the MT and MR, respectively; η_T and η_R are the motion directions of the MT and MR relative to the positive direction of the x-axis, respectively. As shown in Fig. 3, the Rayleigh distance of the RIS-assisted channel model, which differentiates the boundary of the far-field and near-field region, is defined by

$$L_{\text{RIS}} = \frac{2\max\{M^2 d_M^2,\ N^2 d_N^2\}}{\lambda}. \tag{1}$$

Owing to the mobility of the MT and MR, the distance $\xi_{\text{RIS}}^{\text{ter}}(t)$ may be smaller than the Rayleigh distance L_{RIS}, i.e., $\xi_{\text{RIS}}^{\text{ter}}(t) < L_{\text{RIS}}$. In this case, the MT and(or) MR will be in the near-field region of the RIS, and therefore the far-field planar wavefront assumption no longer holds. This motivates us divide the entire RIS array evenly into $M^{\text{sub}}(t) \times N^{\text{sub}}(t)$ sub-arrays with the largest sub-array consisting of $M_x^{\text{sub}}(t) \times N_z^{\text{sub}}(t)$ RIS units, as shown in Fig. 2. To enable the far-field planar wavefront

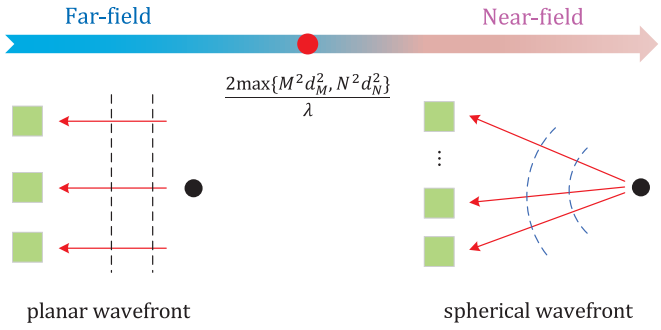

Fig. 3. Illustration of the planar and spherical wavefronts in the proposed RIS-assisted channel model. The circles in black are antenna elements, the squares in green are user terminals, the arrow in red is the transmitted signal, and the dotted lines are wavefronts.

assumption applicable for every sub-array, the dimension of the largest sub-array should satisfy the following constraint:

$$\xi_{\text{RIS}}^{\text{ter}}(t) \geq \frac{2}{\lambda}\max\left\{\left(M_x^{\text{sub}}(t)d_M\right)^2,\ \left(N_z^{\text{sub}}(t)d_N\right)^2\right\}, \quad (2)$$

which yields

$$M_x^{\text{sub}}(t) \leq \sqrt{\frac{\lambda\xi_{\text{RIS}}^{\text{ter}}(t)}{2d_M^2}}, \quad (3)$$

$$N_z^{\text{sub}}(t) \leq \sqrt{\frac{\lambda\xi_{\text{RIS}}^{\text{ter}}(t)}{2d_N^2}}, \quad (4)$$

$$M^{\text{sub}}(t) = \frac{M - \text{mod}\left(M,\ M_x^{\text{sub}}(t)\right)}{M_x^{\text{sub}}(t)} + 1, \quad (5)$$

$$N^{\text{sub}}(t) = \frac{N - \text{mod}\left(N,\ N_z^{\text{sub}}(t)\right)}{N_z^{\text{sub}}(t)} + 1. \quad (6)$$

Meanwhile, the number of columns or rows in any sub-array should be smaller than those in the entire RIS, i.e., $M_x^{\text{sub}}(t) \leq M$ and $N_z^{\text{sub}}(t) \leq N$. Therefore, the proposed sub-array partitioning scheme can be summarized as

$$M_x^{\text{sub}}(t) = \min\left\{\left\lfloor\sqrt{\frac{\lambda\xi_{\text{RIS}}^{\text{ter}}(t)}{2d_M^2}}\right\rfloor,\ M\right\}, \quad (7)$$

$$N_z^{\text{sub}}(t) = \min\left\{\left\lfloor\sqrt{\frac{\lambda\xi_{\text{RIS}}^{\text{ter}}(t)}{2d_N^2}}\right\rfloor,\ N\right\}, \quad (8)$$

$$M^{\text{sub}}(t) = \begin{cases} \dfrac{M - \text{mod}\left(M,\ M_x^{\text{sub}}(t)\right)}{M_x^{\text{sub}}(t)} + 1, \text{if } g_1 \neq 0 \\ \dfrac{M}{M_x^{\text{sub}}(t)}, \text{if } g_1 = 0\ , \end{cases} \quad (9)$$

$$N^{\text{sub}}(t) = \begin{cases} \dfrac{N - \text{mod}\left(N,\ N_z^{\text{sub}}(t)\right)}{N_z^{\text{sub}}(t)} + 1, \text{if } g_2 \neq 0 \\ \dfrac{N}{N_z^{\text{sub}}(t)}, \text{if } g_2 = 0\ , \end{cases} \quad (10)$$

where $g_1 = \text{mod}\left(M,\ M_x^{\text{sub}}(t)\right)$ and $g_2 = \text{mod}\left(N,\ N_z^{\text{sub}}(t)\ \right)$. It is known that when $\xi_{\text{RIS}}^{\text{ter}}(t) \geq L_{\text{RIS}}$, i.e., the MT and MR are in the far-field region of the RIS, the planar wavefront assumption can be applied to the entire RIS and hence no sub-array partition is required. As a result, the expressions (7)-(10) yeild $M_x^{\text{sub}}(t) = M$, $N_z^{\text{sub}}(t) = N$, and $M^{\text{sub}}(t) = N^{\text{sub}}(t) = 1$, which is in agreement with the fact.

In general, the number of RIS units, i.e., M and N, could be set arbitrarily in this paper. This means that different sub-arrays could have different numbers of RIS units, which shows the generality of the proposed scheme. Specifically, the number of RIS units of the $\left(m^{\text{sub}}, n^{\text{sub}}\right)$-th $\left(m^{\text{sub}} = 1, 2, \ldots, M^{\text{sub}}(t)\right.$ and $\left.n^{\text{sub}} = 1, 2, \ldots, N^{\text{sub}}(t)\ \right)$ sub-array can be expressed as

$$M_{m^{\text{sub}}}(t) = \begin{cases} M_x^{\text{sub}}(t), \text{if } 1 \leq m^{\text{sub}} < M^{\text{sub}}(t) \\ M - \left(M^{\text{sub}}(t)\ - 1\right)M_x^{\text{sub}}(t)\ , \text{if } m^{\text{sub}} = M^{\text{sub}}(t) \end{cases}, \quad (11)$$

$$N_{n^{\text{sub}}}(t) = \begin{cases} N_z^{\text{sub}}(t), \text{if } 1 \leq n^{\text{sub}} < N^{\text{sub}}(t) \\ N - \left(N^{\text{sub}}(t)\ - 1\right)N_z^{\text{sub}}(t)\ , \text{if } n^{\text{sub}} = N^{\text{sub}}(t) \end{cases}. \quad (12)$$

In this case, the distance vector from the origin of the global coordinate system to the center of the $(m^{\text{sub}}, n^{\text{sub}})$-th sub-array in RIS can be written by

$$\mathbf{d}_{(m^{\text{sub}},n^{\text{sub}})}^{\text{origin}}(t) = \begin{bmatrix} d_{(m^{\text{sub}},n^{\text{sub}}),x}(t) \\ d_{(m^{\text{sub}},n^{\text{sub}}),y}(t) \\ d_{(m^{\text{sub}},n^{\text{sub}}),z}(t) \end{bmatrix} = \begin{bmatrix} x_{\text{RIS}} + \frac{1}{2}g_3 d_M \cos\epsilon_{\text{RIS}} \\ y_{\text{RIS}} + \frac{1}{2}g_3 d_M \sin\epsilon_{\text{RIS}} \\ z_{\text{RIS}} - \frac{1}{2}g_4 d_N \end{bmatrix}, \quad (13)$$

where $g_3 = 2(m^{\text{sub}} - 1)M_x^{\text{sub}}(t)\ + M_{m^{\text{sub}}}(t) - M$, $g_4 = 2(n^{\text{sub}} - 1)N_z^{\text{sub}}(t)\ + N_{n^{\text{sub}}}(t) - N$, and ϵ_{RIS} denotes the horizontal rotation angle of the RIS. It is worth noting that the proposed sub-array partitioning scheme in this paper is a software-level method, which implies that the sub-arrays can be repartitioned dynamically to accommodate the motion of the MT and MR. Since the ultra massive MIMO technology has been considered promising in the next generation wireless networks, the dimension of the antenna arrays at the transmitter and(or) receiver cannot be ignored. The proposed sub-array partitioning scheme, as a result, can be extended to divide the large antenna arrays at the transmitter and receiver in ultra massive MIMO systems into small sub-arrays to reduce the modeling complexity, which will be our future work.

B. Complex Channel Impulse Response

In the existing literature, the authors have derived the complex channel impulse responses (CIRs) to investigate the RIS-assisted channel characteristics. Here, if we adopt the planar wavefront model to investigate the propagation characteristics as the RIS-assisted channel is in the near-field propagation condition, it will cause low modeling accuracy. However, if we use the spherical wavefront model to study the RIS-assisted channel characteristics in the far-field propagation condition, the modeling complexity will be very high. Furthermore, it is worth noting that the far- and near-field conditions alternately appear in the RIS-assisted mobile communication scenarios, as shown in Fig. 2. Therefore, we propose a dynamic sub-array partitioning scheme for achieving the balance between

the modeling accuracy and complexity of the investigation of the RIS-assisted V2V channel characteristics, which provides a theoretical guidelines for the design and evaluation of the RIS-assisted V2V communication systems. In the proposed channel model, some propagated waves that take place via the RIS and clusters are assumed to be independent to each other. We denote $\mathbf{H}_{\text{TR}}(t)$ as the small-scale fading between different antenna pairs, which can be represented by a $Q \times P$ complex matrix, i.e., $\mathbf{H}_{\text{TR}}(t) = \left[h_{pq}(t,\tau)\right]_{Q\times P}$. Specifically, $h_{pq}(t,\tau)$ denotes the complex CIR between the p-th ($p = 1, 2, \ldots, M_T$) MT antenna and q-th ($q = 1, 2, \ldots, M_R$) MR antenna of the propagation links in the channel model, which is expressed as [25]

$$\begin{aligned} h_{pq}(t,\tau) &= \sqrt{\frac{K}{K+1}} h_{pq}^{\text{RIS}}(t)\delta\Big(\tau - \frac{\xi_{T,\text{RIS}}(t)+\xi_{R,\text{RIS}}(t)}{c}\Big) \\ &+ \sqrt{\frac{1}{K+1}} h_{pq}^{\text{cluster}}(t)\delta\Big(\tau - \frac{\xi_{T,\text{cluster}}(t)+\xi_{R,\text{cluster}}(t)}{c}\Big), \end{aligned} \tag{14}$$

where K denotes the Rician factor, c is the speed of light, $\xi_{T,\text{cluster}}(t)$ and $\xi_{R,\text{cluster}}(t)$ are the time-varying propagation distances from the centers of the MT and MR antenna arrays to that of the cluster, which can be respectively derived by taking the magnitude of the $\xi_{T,\text{cluster}}(t) = \| \mathbf{d}_{T,\text{cluster}}(t) \|$ and $\xi_{R,\text{cluster}}(t) = \| \mathbf{d}_{R,\text{cluster}}(t) \|$, i.e.,

$$\mathbf{d}_{T,\text{cluster}}(t) = \begin{bmatrix} g_{5x} - d_{T,x}(t) \\ g_{5y} - d_{T,y}(t) \\ \xi_{T,\text{cluster}}(0)\sin\beta_{T,\text{cluster}}(0) \end{bmatrix}, \tag{15}$$

$$\mathbf{d}_{R,\text{cluster}}(t) = \begin{bmatrix} g_{6x} - D_0 - d_{R,x}(t) \\ g_{6y} - d_{R,y}(t) \\ \xi_{R,\text{cluster}}(0)\sin\beta_{R,\text{cluster}}(0) \end{bmatrix}, \tag{16}$$

where $g_{5x} = \xi_{T,\text{cluster}}(0)\cos\beta_{T,\text{cluster}}(0)\cos\alpha_{T,\text{cluster}}(0)$, $g_{5y} = \xi_{T,\text{cluster}}(0)\cos\beta_{T,\text{cluster}}(0)\sin\alpha_{T,\text{cluster}}(0)$, $g_{6x} = \xi_{R,\text{cluster}}(0)\cos\beta_{R,\text{cluster}}(0)\cos\alpha_{R,\text{cluster}}(0)$, and $g_{6y} = \xi_{R,\text{cluster}}(0)\cos\beta_{R,\text{cluster}}(0)\sin\alpha_{R,\text{cluster}}(0)$, respectively. The $\alpha_{T,\text{cluster}}(0)$ and $\beta_{T,\text{cluster}}(0)$ are respectively the azimuth angle of departure (AAoD) and elevation angle of departure (EAoD) of the waves from the MT to the center of the cluster; $\alpha_{R,\text{cluster}}(0)$ and $\beta_{R,\text{cluster}}(0)$ are respectively the azimuth angle of arrival (AAoA) and elevation angle of arrival (EAoA) of the waves scattered from the cluster. The $\xi_{T,\text{cluster}}(0)$ and $\xi_{R,\text{cluster}}(0)$ are the distances from the center points of the MT and MR antenna arrays to that of the cluster in the preliminary motion stage, that is, $t = 0$, which can be respectively derived by

$$\xi_{T,\text{cluster}}(0) = \sqrt{x_{\text{cluster}}^2 + y_{\text{cluster}}^2 + z_{\text{cluster}}^2}, \tag{17}$$

$$\xi_{R,\text{cluster}}(0) = \sqrt{(x_{\text{cluster}} - D_0)^2 + y_{\text{cluster}}^2 + z_{\text{cluster}}^2}, \tag{18}$$

where x_{cluster}, y_{cluster}, and z_{cluster} denote the coordinate of the cluster in the x-, y-, and z-th axes, respectively.

For the RIS propagation link, the channel coefficient $h_{pq}^{\text{RIS}}(t)$ for the (p,q)-th antenna pair can be expressed as

$$\begin{aligned} h_{pq}^{\text{RIS}}(t) &= \sqrt{\frac{1}{\Upsilon_{pq}(t)}} \sum_{m=1}^{M}\sum_{n=1}^{N} \chi_{m,n}(t) \\ &\times e^{j\left(\varphi_{m,n}(t) - \frac{2\pi}{\lambda}\left(\xi_{T,(m,n)}(t)+\xi_{R,(m,n)}(t)\right)\right)} \\ &\times e^{j\frac{2\pi}{\lambda}k_p\delta_T\cos\left(\alpha_{T,(m,n)}(t)-\psi_T\right)\cos\beta_{T,(m,n)}(t)\cos\theta_T} \\ &\times e^{j\frac{2\pi}{\lambda}k_p\delta_T\sin\beta_{T,(m,n)}(t)\sin\theta_T} \\ &\times e^{j\frac{2\pi}{\lambda}k_q\delta_R\cos\left(\alpha_{R,(m,n)}(t)-\psi_R\right)\cos\beta_{R,(m,n)}(t)\cos\theta_R} \\ &\times e^{j\frac{2\pi}{\lambda}k_q\delta_R\sin\beta_{R,(m,n)}(t)\sin\theta_R} \\ &\times e^{j\frac{2\pi}{\lambda}v_T t\cos\left(\alpha_{T,(m,n)}(t)-\eta_T\right)\cos\beta_{T,(m,n)}(t)} \\ &\times e^{j\frac{2\pi}{\lambda}v_R t\cos\left(\alpha_{R,(m,n)}(t)-\eta_R\right)\cos\beta_{R,(m,n)}(t)}, \end{aligned} \tag{19}$$

where $k_p = (P - 2p + 1)/2$ and $k_q = (Q - 2q + 1)/2$. In (19), $\chi_{m,n}(t)$ and $\varphi_{m,n}(t)$ are respectively the reflection amplitude and phase of the (m,n)-th unit in RIS. It is worth mentioning that when the random phase regulation is uniform, it is reasonable to assume that the $\varphi_{m,n}(t)$ follows the uniform distribution. However, when the phase regulation is discrete, the $\varphi_{m,n}(t)$ can be defined as some discrete values. Furthermore, $\Upsilon_{pq}(t)$ is the normalized factor of the RIS link to make $h_{pq}^{\text{RIS}}(t)$ with unit power, which can be expressed as

$$\begin{aligned} \Upsilon_{pq}(t) = \mathbb{E}\Big\{\Big| & e^{j\left(\varphi_{m,n}(t) - \frac{2\pi}{\lambda}\left(\xi_{T,(m,n)}(t)+\xi_{R,(m,n)}(t)\right)\right)} \\ &\times e^{j\frac{2\pi}{\lambda}k_p\delta_T\cos\left(\alpha_{T,(m,n)}(t)-\psi_T\right)\cos\beta_{T,(m,n)}(t)\cos\theta_T} \\ &\times e^{j\frac{2\pi}{\lambda}k_p\delta_T\sin\beta_{T,(m,n)}(t)\sin\theta_T} \\ &\times e^{j\frac{2\pi}{\lambda}k_q\delta_R\cos\left(\alpha_{R,(m,n)}(t)-\psi_R\right)\cos\beta_{R,(m,n)}(t)\cos\theta_R} \\ &\times e^{j\frac{2\pi}{\lambda}k_q\delta_R\sin\beta_{R,(m,n)}(t)\sin\theta_R} \\ &\times e^{j\frac{2\pi}{\lambda}v_T t\cos\left(\alpha_{T,(m,n)}(t)-\eta_T\right)\cos\beta_{T,(m,n)}(t)} \\ &\times e^{j\frac{2\pi}{\lambda}v_R t\cos\left(\alpha_{R,(m,n)}(t)-\eta_R\right)\cos\beta_{R,(m,n)}(t)}\Big|^2\Big\}. \end{aligned} \tag{20}$$

where $\mathbb{E}[\cdot]$ represents the expectation operation, which applies to the reflection phase $\varphi_{m,n}(t)$ for the RIS propagation links. In the proposed channel model, the initial distance/angle/delay parameters can be determined once the geometric setups among the MT, RIS, and MR is confirmed from a measurement campaign or generated randomly [8]. The values of these model parameters after a time interval of t can be derived by exploiting the geometric relationships among the MT, RIS, and MR according to the initial parameters values and the motion speeds/directions/time of the MT and MR [16]. Specifically, we take the center point of the sub-array as the reference point when deriving the model parameters, the time-varying distance from the center of MT and MR antenna arrays to the (m,n)-th unit in the $\left(m^{\text{sub}}, n^{\text{sub}}\right)$-th sub-array in RIS can be respectively expressed as (21) and (22), shown at the bottom of the next page, respectively, where $(m^{\text{sub}} - 1)M_x^{\text{sub}}(t) + 1 \le m \le (m^{\text{sub}} - 1)M_x^{\text{sub}}(t) + M_{m^{\text{sub}}}(t)$ and $(n^{\text{sub}} - 1)N_z^{\text{sub}}(t) + 1 \le n \le (n^{\text{sub}} - 1)N_z^{\text{sub}}(t) + N_{n^{\text{sub}}}(t)$ limit the indexes of RIS units in the range of $\left(m^{\text{sub}}, n^{\text{sub}}\right)$-th sub-array of RIS. The $\alpha_{m,n}^{\text{in}}(t)$ and $\beta_{m,n}^{\text{in}}(t)$ are respectively the azimuth and normal incident angles from the MT to (m,n)-th unit; $\alpha_{m,n}^{\text{out}}(t)$ and $\beta_{m,n}^{\text{out}}(t)$ are respectively the azimuth and normal reflected angles from (m,n)-th unit to the MR. Their derivations will be discussed in Appendix A. It is worth mentioning that all the RIS units in the same sub-array share the same signal angles; therefore, for $m - (m^{\text{sub}} - 1)M_x^{\text{sub}}(t) \in \{1, 2, \ldots M_{m^{\text{sub}}}(t)\}$ and $n - (n^{\text{sub}} - 1)N_z^{\text{sub}}(t) \in \{1, 2, \ldots N_{n^{\text{sub}}}(t)\}$, the

time-varying AAoD and EAoD of the waves from the MT to the (m,n)-th unit in RIS can be expressed as (23) and (24), respectively, where (24), shown at the bottom of the page.

$$\alpha_{T,(m,n)}(t) = \arctan \frac{d_{(m^{\text{sub}},n^{\text{sub}}),y}(t) - d_{T,y}(t)}{d_{(m^{\text{sub}},n^{\text{sub}}),x}(t) - d_{T,x}(t)}. \tag{23}$$

At the MR, the time-varying AAoA and EAoA from the (m,n)-th unit in RIS to the MR can be expressed as (25) and (26), respectively, where (26), shown at the bottom of the page.

$$\alpha_{R,(m,n)}(t) = \arctan \frac{d_{(m^{\text{sub}},n^{\text{sub}}),y}(t) - D_0 - d_{R,y}(t)}{d_{(m^{\text{sub}},n^{\text{sub}}),x}(t) - d_{R,x}(t)}. \tag{25}$$

For the NLoS propagation link, the channel coefficient $h_{pq}^{\text{cluster}}(t)$ of the link that is independent of the NLoS link, can be expressed as

$$\begin{aligned} h_{pq}^{\text{cluster}}(t) = & \frac{1}{\sqrt{L}} \sum_{\ell=1}^{L} e^{j\left(\varphi_\ell - \frac{2\pi}{\lambda}\left(\xi_{T,\text{cluster},\ell}(t) + \xi_{R,\text{cluster},\ell}(t)\right)\right)} \\ & \times e^{j\frac{2\pi}{\lambda} k_p \delta_T \cos\left(\alpha_{T,\text{cluster},\ell}(t) - \psi_T\right) \cos\beta_{T,\text{cluster},\ell}(t) \cos\theta_T} \\ & \times e^{j\frac{2\pi}{\lambda} k_p \delta_T \sin\beta_{T,\text{cluster},\ell} \sin\theta_T} \\ & \times e^{j\frac{2\pi}{\lambda} k_q \delta_R \cos\left(\alpha_{R,\text{cluster},\ell}(t) - \psi_R\right) \cos\beta_{R,\text{cluster},\ell}(t) \cos\theta_R} \\ & \times e^{j\frac{2\pi}{\lambda} k_q \delta_R \sin\beta_{R,\text{cluster},\ell}(t) \sin\theta_R} \\ & \times e^{j\frac{2\pi}{\lambda} v_T t \cos\left(\alpha_{T,\text{cluster},\ell}(t) - \eta_T\right) \cos\beta_{T,\text{cluster},\ell}(t)} \\ & \times e^{j\frac{2\pi}{\lambda} v_R t \cos\left(\alpha_{R,\text{cluster},\ell}(t) - \eta_R\right) \cos\beta_{R,\text{cluster},\ell}(t)}, \end{aligned} \tag{27}$$

where L denotes the number of NLoS rays within the cluster, which is generally assumed to be a very large number approaching infinity, i.e., $L \to \infty$, and $\{\varphi_\ell\}_{\ell=1,2,\ldots L}$ are assumed to be independent and uniformly distributed random phases, that is, $\varphi_\ell \sim \text{U}[-\pi,\pi)$. The scatterers within the same cluster are assumed to have approximately the same initial distance to the center of MR antenna array but with different angles, i.e., $\xi_{R,\text{cluster}}(0) \approx \xi_{R,\text{cluster},1}(0) \cdots \approx \xi_{R,\text{cluster},\ell}(0) \cdots \approx \xi_{R,\text{cluster},L}(0)$ [26]. Then, the time-varying distances from the centers of the MT and MR antenna arrays to the ℓ-th scatterer within the cluster can be respectively derived by taking the magnitude of the $\xi_{T,\text{cluster},\ell}(t) = \| \mathbf{d}_{T,\text{cluster},\ell}(t) \|$ and $\xi_{R,\text{cluster},\ell}(t) = \| \mathbf{d}_{R,\text{cluster},\ell}(t) \|$, i.e.,

$$\mathbf{d}_{T,\text{cluster},\ell}(t) = \begin{bmatrix} g_{7x} - d_{T,x}(t) \\ g_{7y} - d_{T,y}(t) \\ \xi_{T,\text{cluster}}(0) \sin\beta_{T,\text{cluster},\ell}(0) \end{bmatrix}, \tag{28}$$

$$\mathbf{d}_{R,\text{cluster},\ell}(t) = \begin{bmatrix} g_{8x} - D_0 - d_{R,x}(t) \\ g_{8y} - d_{R,y}(t) \\ \xi_{R,\text{cluster}}(0) \sin\beta_{R,\text{cluster},\ell}(0) \end{bmatrix}. \tag{29}$$

where $g_{7x} = \xi_{T,\text{cluster}}(0) \cos\beta_{T,\text{cluster},\ell}(0) \cos\alpha_{T,\text{cluster},\ell}(0)$, $g_{7y} = \xi_{T,\text{cluster}}(0) \cos\beta_{T,\text{cluster},\ell}(0) \sin\alpha_{T,\text{cluster},\ell}(0)$, $g_{8x} = \xi_{R,\text{cluster}}(0) \cos\beta_{R,\text{cluster},\ell}(0) \cos\alpha_{R,\text{cluster},\ell}(0)$, and $g_{8y} = \xi_{R,\text{cluster}}(0) \cos\beta_{R,\text{cluster},\ell}(0) \sin\alpha_{R,\text{cluster},\ell}(0)$, respectively. Furthermore, the time-varying AAoD and EAoD of the waves from the MT to the ℓ-th scatterer can be respectively expressed as

$$\alpha_{T,\text{cluster},\ell}(t) = \arctan \frac{g_{7y} - d_{T,y}(t)}{g_{7x} - d_{T,x}(t)}, \tag{30}$$

$$\beta_{T,\text{cluster},\ell}(t) = \text{arccot} \frac{\sqrt{(g_{7x} - d_{T,x}(t))^2 + (g_{7y} - d_{T,y}(t))^2}}{\xi_{T,\text{cluster}}(0) \sin\beta_{T,\text{cluster},\ell}(0)}. \tag{31}$$

The time-varying AAoA and EAoA of the waves from the ℓ-th scatterer to the MR can be respectively expressed as

$$\alpha_{R,\text{cluster},\ell}(t) = \arctan \frac{g_{8y} - d_{R,y}(t)}{g_{8x} - D_0 - d_{R,x}(t)}, \tag{32}$$

$$\beta_{R,\text{cluster},\ell}(t) = \text{arccot} \frac{\sqrt{(g_{8x} - D_0 - d_{R,x}(t))^2 + (g_{8y} - d_{R,y}(t))^2}}{\xi_{R,\text{cluster}}(0) \sin\beta_{R,\text{cluster},\ell}(0)}. \tag{33}$$

III. Statistical Properties of the Proposed Channel Model

Based on the proposed sub-array pattern scheme, we in this section will derive and investigate the RIS-assisted V2V

$$\begin{aligned} \xi_{T,(m,n)}(t) \approx & \left\| \mathbf{d}_T(t) - \mathbf{d}^{\text{origin}}_{(m^{\text{sub}},n^{\text{sub}})}(t) \right\| - \frac{1}{2}\left((m - (m^{\text{sub}}-1)M_x^{\text{sub}}(t)) - M_{m^{\text{sub}}}(t) - 1\right) d_M \sin\beta^{\text{in}}_{m,n}(t) \cos\alpha^{\text{in}}_{m,n}(t) \\ & + \frac{1}{2}\left((n - (n^{\text{sub}}-1)N_z^{\text{sub}}(t)) - N_{n^{\text{sub}}}(t) - 1\right) d_N \sin\beta^{\text{in}}_{m,n}(t) \sin\alpha^{\text{in}}_{m,n}(t), \end{aligned} \tag{21}$$

$$\begin{aligned} \xi_{R,(m,n)}(t) \approx & \left\| \mathbf{d}_R(t) - \mathbf{d}^{\text{origin}}_{(m^{\text{sub}},n^{\text{sub}})}(t) \right\| - \frac{1}{2}\left((m - (m^{\text{sub}}-1)M_x^{\text{sub}}(t)) - M_{m^{\text{sub}}}(t) - 1\right) d_M \sin\beta^{\text{out}}_{m,n}(t) \cos\alpha^{\text{out}}_{m,n}(t) \\ & + \frac{1}{2}\left((n - (n^{\text{sub}}-1)N_z^{\text{sub}}(t)) - N_{n^{\text{sub}}}(t) - 1\right) d_N \sin\beta^{\text{out}}_{m,n}(t) \sin\alpha^{\text{out}}_{m,n}(t). \end{aligned} \tag{22}$$

$$\beta_{T,(m,n)}(t) = \arctan \frac{d_{(m^{\text{sub}},n^{\text{sub}}),z}(t)}{\sqrt{\left(d_{(m^{\text{sub}},n^{\text{sub}}),x}(t) - d_{T,x}(t)\right)^2 + \left(d_{(m^{\text{sub}},n^{\text{sub}}),y}(t) - d_{T,y}(t)\right)^2}}. \tag{24}$$

$$\beta_{R,(m,n)}(t) = \arctan \frac{d_{(m^{\text{sub}},n^{\text{sub}}),z}(t)}{\sqrt{\left(d_{(m^{\text{sub}},n^{\text{sub}}),x}(t) - D_0 - d_{R,x}(t)\right)^2 + \left(d_{(m^{\text{sub}},n^{\text{sub}}),y}(t) - d_{R,y}(t)\right)^2}}. \tag{26}$$

channel propagation characteristics, including those of the ST CCFs, temporal ACFs, and FCFs.

A. ST CCFs

In the proposed channel model, the normalized ST CCF is defined as the correlation between two different channel coefficients $h_{pq}(t)$ and $h_{p'q'}(t+\Delta t)$, where $p' = 1, 2, \ldots, M_T$ and $q' = 1, 2, \ldots, M_R$. Therefore, we have [15]

$$\rho_{(p,q),(p',q')}(t, \Delta p, \Delta q, \Delta t) = \frac{\mathbb{E}\left[h^*_{pq}(t) h_{p'q'}(t+\Delta t)\right]}{\sqrt{\mathbb{E}\left[|h_{pq}(t)|^2\right]\mathbb{E}\left[|h_{p'q'}(t+\Delta t)|^2\right]}}, \tag{34}$$

where Δt denotes the time difference, $\Delta p = |k_{p'} - k_p|\delta_T/\lambda$ and $\Delta q = |k_{q'} - k_q|\delta_R/\lambda$ are respectively the normalized antenna spacings of the MT and MR antenna arrays, and p, p', q, and q' are the antenna indexes.

By substituting (19) and (27) into (34), we can further express the ST CCF between the (p, q)-th antenna pair and the (p', q')-th antenna pair of the propagation links in the proposed channel model as follows:

$$\begin{aligned}\rho_{(p,q),(p',q')}(t, \Delta p, \Delta q, \Delta t) &= \rho^{\text{RIS}}_{(p,q),(p',q')}(t, \Delta p, \Delta q, \Delta t) \\ &+ \rho^{\text{cluster}}_{(p,q),(p',q')}(t, \Delta p, \Delta q, \Delta t),\end{aligned} \tag{35}$$

where $\rho^{\text{RIS}}_{(p,q),(p',q')}(t, \Delta p, \Delta q, \Delta t)$ denotes the ST CCF between the RIS propagation links, which can be expressed as

$$\begin{aligned}&\rho^{\text{RIS}}_{(p,q),(p',q')}(t, \Delta p, \Delta q, \Delta t) \\ &= \frac{K}{K+1} \times \frac{1}{\sqrt{\Upsilon_{pq}(t)\Upsilon_{p'q'}(t+\Delta t)}} \\ &\times \mathbb{E}\Big\{ \sum_{m=1}^{M}\sum_{n=1}^{N}\sum_{m'=1}^{M}\sum_{n'=1}^{N} \chi_{mn}(t)\ \chi_{m'n'}(t+\Delta t) \\ &\times e^{j\left(\varphi_{m'n'}(t+\Delta t) - \varphi_{mn}(t)\right)} \\ &\times e^{j\frac{2\pi}{\lambda}\left(\xi_{T,(m,n)}(t) - \xi_{T,(m',n')}(t+\Delta t)\right)} \\ &\times e^{j\frac{2\pi}{\lambda}\left(\xi_{R,(m,n)}(t) - \xi_{R,(m',n')}(t+\Delta t)\right)} \\ &\times e^{-j\frac{2\pi}{\lambda}k_p\delta_T \cos\left(\alpha_{T,(m,n)}(t) - \psi_T\right)\cos\beta_{T,(m,n)}(t)\cos\theta_T} \\ &\times e^{-j\frac{2\pi}{\lambda}k_p\delta_T \sin\beta_{T,(m,n)}(t)\sin\theta_T} \\ &\times e^{j\frac{2\pi}{\lambda}k_{p'}\delta_T \cos\left(\alpha_{T,(m',n')}(t+\Delta t) - \psi_T\right)\cos\beta_{T,(m',n')}(t+\Delta t)\cos\theta_T} \\ &\times e^{j\frac{2\pi}{\lambda}k_{p'}\delta_T \sin\beta_{T,(m',n')}(t+\Delta t)\sin\theta_T} \\ &\times e^{-j\frac{2\pi}{\lambda}k_q\delta_R \cos\left(\alpha_{R,(m,n)}(t) - \psi_R\right)\cos\beta_{R,(m,n)}(t)\cos\theta_R} \\ &\times e^{-j\frac{2\pi}{\lambda}k_q\delta_R \sin\beta_{R,(m,n)}(t)\sin\theta_R} \\ &\times e^{j\frac{2\pi}{\lambda}k_{q'}\delta_R \cos\left(\alpha_{R,(m',n')}(t+\Delta t) - \psi_R\right)\cos\beta_{R,(m',n')}(t+\Delta t)\cos\theta_R} \\ &\times e^{j\frac{2\pi}{\lambda}k_{q'}\delta_R \sin\beta_{R,(m',n')}(t+\Delta t)\sin\theta_R} \\ &\times e^{j\frac{2\pi}{\lambda}v_T(t+\Delta t)\cos\left(\alpha_{T,(m',n')}(t+\Delta t) - \eta_T\right)\cos\beta_{T,(m',n')}(t+\Delta t)} \\ &\times e^{-j\frac{2\pi}{\lambda}v_T t\cos\left(\alpha_{T,(m,n)}(t) - \eta_T\right)\cos\beta_{T,(m,n)}(t)} \\ &\times e^{j\frac{2\pi}{\lambda}v_R(t+\Delta t)\cos\left(\alpha_{R,(m',n')}(t+\Delta t) - \eta_R\right)\cos\beta_{R,(m',n')}(t+\Delta t)} \\ &\times e^{-j\frac{2\pi}{\lambda}v_R t\cos\left(\alpha_{R,(m,n)}(t) - \eta_R\right)\cos\beta_{R,(m,n)}(t)}\Big\}.\end{aligned} \tag{36}$$

It is noteworthy to mention that the time-varying angles $\alpha_{T,(m,n)}(t)$, $\beta_{T,(m,n)}(t)$, $\alpha_{R,(m,n)}(t)$, and $\beta_{R,(m,n)}(t)$ are related to the motion time/directions/velocities of the MT and MR, which implies that the motion properties of the transceivers affect the ST CCFs between different RIS links in the RIS-assisted V2V channel model.

In (35), $\rho^{\text{cluster}}_{(p,q),(p',q')}(t, \Delta p, \Delta q, \Delta t)$ is the ST CCF between different NLoS components via the cluster. Here, we assume that the number of scatterers within the cluster approaches infinity, i.e., $L \to \infty$, the summations of infinite scatterers will be replaced by the integral of $\alpha_{R,\text{cluster}}$ and $\beta_{R,\text{cluster}}$, respectively. Therefore, we have ...

$$\begin{aligned}&\rho^{\text{cluster}}_{(p,q),(p',q')}(t, \Delta p, \Delta q, \Delta t) \\ &= \frac{1}{K+1}\int_{-\pi}^{\pi}\int_{-\pi}^{\pi} \\ &\times e^{j\frac{2\pi}{\lambda}\left(\xi_{T,\text{cluster}}(t) - \xi_{T,\text{cluster}}(t+\Delta t) + \xi_{R,\text{cluster}}(t) - \xi_{R,\text{cluster}}(t+\Delta t)\right)} \\ &\times e^{-j\frac{2\pi}{\lambda}k_p\delta_T \cos\left(\alpha_{T,\text{cluster}}(t) - \psi_T\right)\cos\beta_{T,\text{cluster}}(t)\cos\theta_T} \\ &\times e^{-j\frac{2\pi}{\lambda}k_p\delta_T \sin\beta_{T,\text{cluster}}(t)\sin\theta_T} \\ &\times e^{j\frac{2\pi}{\lambda}k_{p'}\delta_T \cos\left(\alpha_{T,\text{cluster}}(t+\Delta t) - \psi_T\right)\cos\beta_{T,\text{cluster}}(t+\Delta t)\cos\theta_T} \\ &\times e^{j\frac{2\pi}{\lambda}k_{p'}\delta_T \sin\beta_{T,\text{cluster}}(t+\Delta t)\sin\theta_T} \\ &\times e^{-j\frac{2\pi}{\lambda}k_q\delta_R \cos\left(\alpha_{R,\text{cluster}}(t) - \psi_R\right)\cos\beta_{R,\text{cluster}}(t)\cos\theta_R} \\ &\times e^{-j\frac{2\pi}{\lambda}k_q\delta_R \sin\beta_{R,\text{cluster}}(t)\sin\theta_R} \\ &\times e^{j\frac{2\pi}{\lambda}k_{q'}\delta_R \cos\left(\alpha_{R,\text{cluster}}(t+\Delta t) - \psi_R\right)\cos\beta_{R,\text{cluster}}(t+\Delta t)\cos\theta_R} \\ &\times e^{j\frac{2\pi}{\lambda}k_{q'}\delta_R + \sin\beta_{R,\text{cluster}}(t)\sin\theta_R} \\ &\times e^{-j\frac{2\pi}{\lambda}v_T t\cos\left(\alpha_{T,\text{cluster}}(t) - \eta_T\right)\cos\beta_{T,\text{cluster}}(t)} \\ &\times e^{j\frac{2\pi}{\lambda}v_T(t+\Delta t)\cos\left(\alpha_{T,\text{cluster}}(t+\Delta t) - \eta_T\right)\cos\beta_{T,\text{cluster}}(t+\Delta t)} \\ &\times e^{-j\frac{2\pi}{\lambda}v_R t\cos\left(\alpha_{R,\text{cluster},\ell}(t) - \eta_R\right)\cos\beta_{R,\text{cluster}}(t)} \\ &\times e^{j\frac{2\pi}{\lambda}v_R(t+\Delta t)\cos\left(\alpha_{R,\text{cluster}}(t+\Delta t) - \eta_R\right)\cos\beta_{R,\text{cluster}}(t+\Delta t)} \\ &\times f(\alpha_{R,\text{cluster}}, \beta_{R,\text{cluster}}) d(\alpha_{R,\text{cluster}}, \beta_{R,\text{cluster}}),\end{aligned} \tag{37}$$

where $f(\alpha_{R,\text{cluster}}, \beta_{R,\text{cluster}})$ denotes the joint probability density function (PDF) of the received azimuth $\alpha_{R,\text{cluster}}$ and elevation $\beta_{R,\text{cluster}}$ angles. For such propagation, the directions of the rays in each cluster are generally limited to a certain range. Therefore, we adopt the truncated Gaussian distribution to describe the initial azimuth angle distribution, as well as the Laplace distribution to describe the initial elevation angle distribution. The PDFs of the $\alpha_{R,\text{cluster}}$ and $\beta_{R,\text{cluster}}$ can be respectively expressed as (38) and (39), shown at the bottom of the next page, respectively, where $\mu_{\alpha|\beta_{R,\text{cluster}}}$ and $\sigma_{\alpha|\beta_{R,\text{cluster}}} = \alpha|\beta^{\text{up}}_{\alpha_{R,\text{cluster}}} - \alpha|\beta^{\text{low}}_{\alpha_{R,\text{cluster}}}$ are respectively the mean value and angle spread of the signal direction $\alpha|\beta_{R,\text{cluster}} \in \left[\alpha|\beta^{\text{low}}_{\alpha_{R,\text{cluster}}}, \alpha|\beta^{\text{up}}_{\alpha_{R,\text{cluster}}}\right]$. The $u(\varsigma)$ is the PDF of the standard normal distributed random variable ς, which can be expressed as $u(\varsigma) = \frac{1}{\sqrt{2\pi}}\exp\{-\frac{\varsigma^2}{2}\}$, whereas $\Phi(\varsigma) = \int_{-\infty}^{\varsigma} u(\varsigma')d\varsigma' = \frac{1}{2}\left(1 + erf(\frac{\varsigma}{\sqrt{2}})\right)$ represents the cumulative distribution function (CDF) of the standard normal distributed random variable ς with $erf(\cdot)$ being the Gauss error function. Furthermore, $F(\beta, \mu_\beta, \sigma_\beta)$ is the CDF of the Laplace distributed random

variable β with mean value μ_β and variance σ_β^2. Specifically, $F(\beta,\mu_\beta,\sigma_\beta) = \frac{1}{2}\exp\left[-\sqrt{2}\frac{\mu_\beta-\beta}{\sigma_\beta}\right]$ as $\beta \le \mu_\beta$; otherwise, $F(\beta,\mu_\beta,\sigma_\beta) = 1-\frac{1}{2}\exp\left[-\sqrt{2}\frac{\beta-\mu_\beta}{\sigma_\beta}\right]$. Since the signal azimuth and elevation angles are generally assumed to be independent of each other, the joint PDF in (37) can be further expressed as

$$\begin{aligned} &f(\alpha_{R,\text{cluster}},\beta_{R,\text{cluster}}) \\ &= f\left(\alpha_{R,\text{cluster}},\mu_{\alpha_{R,\text{cluster}}},\sigma_{\alpha_{R,\text{cluster}}},\alpha_{R,\text{cluster}}^{\text{low}},\alpha_{R,\text{cluster}}^{\text{up}}\right) \\ &\times f\left(\beta_{R,\text{cluster}},\mu_{\beta_{R,\text{cluster}}},\sigma_{\beta_{R,\text{cluster}}},\beta_{R,\text{cluster}}^{\text{low}},\beta_{R,\text{cluster}}^{\text{up}}\right). \end{aligned} \tag{40}$$

By setting $\Delta t = 0$, the expressions of (35)-(37) can be used to describe the spatial CCFs between different antenna pairs of the propagation links, which reveals the spatial correlation characteristics of the RIS-assisted V2V channel model. By imposing $p = p'$ and $q = q'$, that is, $\Delta p = \Delta q = 0$, on the other hand, the formulas (35)-(37) can be used to describe the temporal ACFs of the RIS/NLoS propagation links at different time instants, which implies the temporal correlation characteristics of the proposed channel model.

B. FCFs

By taking the Fourier transform of the complex CIR $h_{pq}(t,\tau)$ in (14) with respect to the propagation delay τ, the time-varying transfer function for the (p,q)-th antenna pair of the propagation link in the proposed channel model is written by

$$\begin{aligned} H_{pq}(t,f) = &\sqrt{\frac{K}{K+1}}h_{pq}^{\text{RIS}}(t)e^{-j2\pi f\left(\xi_{T,\text{RIS}}(t)+\xi_{R,\text{RIS}}(t)\right)/c} \\ &+\sqrt{\frac{1}{K+1}}h_{pq}^{\text{cluster}}(t)e^{-j2\pi f\left(\xi_{T,\text{cluster}}(t)+\xi_{R,\text{cluster}}(t)\right)/c}. \end{aligned} \tag{41}$$

The normalized FCF of the proposed channel model are defined as

$$\rho_{H_{pq}}(t,\Delta f) = \frac{\mathbb{E}\left[H_{pq}^*(t)H_{p'q'}(f+\Delta f)\right]}{\sqrt{\mathbb{E}\left[|H_{pq}(t)|^2\right]\mathbb{E}\left[|H_{p'q'}(f+\Delta f)|^2\right]}}, \tag{42}$$

where Δf denotes frequency separation. By substituting (41) into (42), the FCFs of the proposed channel model can be expressed as

$$\begin{aligned} \rho_{H_{pq}}(t,\Delta f) = &\frac{K}{K+1}e^{-j2\pi\Delta f\left(\xi_{T,\text{RIS}}(t)+\xi_{R,\text{RIS}}(t)\right)/c} \\ &+\frac{1}{K+1}\sum_{\ell=1}^{L}e^{-j2\pi\Delta f\left(\xi_{T,\text{cluster}}(t)+\xi_{R,\text{cluster}}(t)\right)/c}. \end{aligned} \tag{43}$$

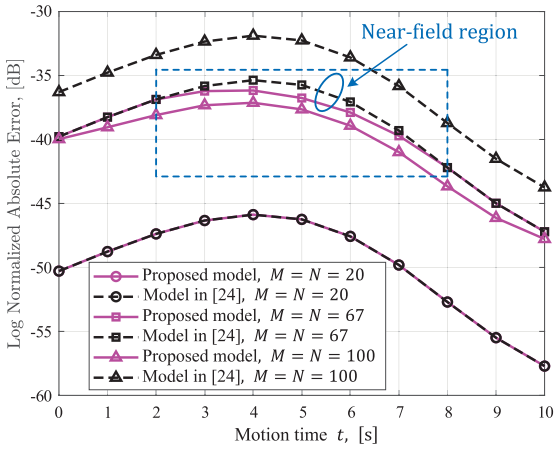

Fig. 4. RIS-assisted V2V channel modeling errors based on the proposed sub-array pattern scheme and conventional method with respect to the number of RIS units when $v_T = 5$ m/s, $v_R = 5$ m/s, $\eta_T = 0$, and $\eta_R = \pi$.

It is noteworthy to mention that the FCF of the proposed RIS-assisted V2V channel model is related to the motion time t but independent of the frequency f, which indicates that the channel model is non-stationary in time domain while stationary in frequency domain. Furthermore, it implies that the physical properties of the RIS will also play a role in the frequency correlations through the propagation delays, which is a specific feature of the RIS-assisted V2V channels.

IV. Numerical Results and Discussions

A. Simulation Setup

Based on the derivations in Section III, the parameters for computer simulations are listed here unless specified otherwise: $f_c = 5.9$ GHz, $M_T = 4$, $M_R = 6$, $\delta_T = \lambda/2$, $\delta_R = \lambda/2$, $\psi_T = \pi/3$, $\theta_T = \pi/4$, $\psi_R = \pi/4$, $\theta_R = \pi/4$, and $D_0 = 100$ m. For NLoS link, we set $\alpha_{R,\text{cluster}} = 2\pi/3$, $\mu_{\alpha_{R,\text{cluster}}} = \pi/6$, $\beta_{R,\text{cluster}} = \pi/4$, $\mu_{\beta_{R,\text{cluster}}} = \pi/12$. For RIS link, we set $x_{\text{RIS}} = 25$ m, $y_{\text{RIS}} = 20$ m, $z_{\text{RIS}} = 15$ m, $M = N = 100$, $d_M = d_N = \lambda/4$, and $\epsilon_{\text{RIS}} = -\pi/18$. For the RIS reflection coefficient, we set $\chi_{m,n}(t) = 1$ and assume optimal reflection phase configuration.

B. Accuracy of Channel Modeling

In Fig. 4, we analyze the channel modeling performance of the proposed sub-array partition based channel modeling solution for RIS-assisted communications by comparing with existing models that are based on far-field planar wavefront assumption [24]. In the simulations, we adopt the ray-tracing

$$f\left(\alpha_{R,\text{cluster}},\mu_{\alpha_{R,\text{cluster}}},\sigma_{\alpha_{R,\text{cluster}}},\alpha_{R,\text{cluster}}^{\text{low}},\alpha_{R,\text{cluster}}^{\text{up}}\right) = \frac{1}{\sigma_{\alpha_{R,\text{cluster}}}} \times \frac{u\left(\frac{\alpha_{R,\text{cluster}}-\mu_{\alpha_{R,\text{cluster}}}}{\sigma_{\alpha_{R,\text{cluster}}}}\right)}{\Phi\left(\frac{\alpha_{R,\text{cluster}}^{\text{up}}-\mu_{\alpha_{R,\text{cluster}}}}{\sigma_{\alpha_{R,\text{cluster}}}}\right)-\Phi\left(\frac{\alpha_{R,\text{cluster}}^{\text{low}}-\mu_{\alpha_{R,\text{cluster}}}}{\sigma_{\alpha_{R,\text{cluster}}}}\right)}, \tag{38}$$

$$f(\beta_{R,\text{cluster}},\mu_{\beta_{R,\text{cluster}}},\sigma_{\beta_{R,\text{cluster}}},\beta_{R,\text{cluster}}^{\text{low}},\beta_{R,\text{cluster}}^{\text{up}}) = \frac{\frac{1}{\sqrt{2}\sigma_{\beta_{R,\text{cluster}}}}\exp\left\{-\frac{\sqrt{2}\left|\beta_{R,\text{cluster}}-\mu_{\beta_{R,\text{cluster}}}\right|}{\sigma_{\beta_{R,\text{cluster}}}}\right\}}{F(\beta_{R,\text{cluster}}^{\text{up}},\mu_{\beta_{R,\text{cluster}}},\sigma_{\beta_{R,\text{cluster}}})-F(\beta_{R,\text{cluster}}^{\text{low}},\mu_{\beta_{R,\text{cluster}}},\sigma_{\beta_{R,\text{cluster}}})}, \tag{39}$$

model, which assumes that different RIS units have different angle parameters, as the baseline model to calculate the channel modeling error. The results show that as the RIS units number increases, which corresponds to increasing RIS array dimension, the proposed model and the model in [24] have different channel modeling error performance. Specifically, when the RIS units number is relatively small, i.e., $M = N = 20$, which is a small size of the RIS array, the proposed model and the model in [24] show the same channel modeling error performance. This can be interpreted by the fact that a small sized RIS array have a shorter Rayleigh distance, so that the MT/MR are always in the far-field region of the RIS under the considered mobility trajectory, making the proposed model to be a far-field model. When a relatively large sized RIS is considered, i.e., $M = N = 100$, on the other hand, the Rayleigh distance of the RIS is large enough so that the MT/MR are always in the near-field region of the RIS. In this case, the proposed model outperforms the far-field model in [24] thanks to the consideration of sub-array partition. Moreover, by comparing the curves with $M = N = 67$, we observe that as the moving time t increases, the channel modeling error performance of the proposed model and the far-field model in [24] are the same firstly, then become different from $t \approx 2$ s, and finally return to be the same again from $t \approx 8$ s. This is because that the MT is firstly in the far-field region of the RIS with $M = N = 67$, thus the proposed model and the far-field model in [24] show the same performance. As the t increases, the distance between MT and RIS becomes shorter than the Rayleigh distance of RIS and the MT moves into the near-field region of the RIS, making the far-field model in [24] suffer from larger modeling error. When $t > 8$ s, the MT moves out of the near-field region of the RIS, and the far-field assumption can be re-applied, resulting in the same modeling error performance between the proposed model and the model in [24]. This phenomenon of the alternating appearance of the far-field or near-field propagation is a unique and commom property in future RIS-assisted mobile communication networks. The proposed sub-array partition based channel modeling scheme can be an efficient solution to meet this requirement.

Fig. 5 shows the channel modeling error performance of the proposed sub-array partition based modeling solution with respect to increasing RIS array dimension under different moving time instants. It can be seen that the channel modeling errors behave differently at distinct time instants owing to the different distances between the RIS and the terminals (MT and MR). This is because that when the RIS array dimension is small, the distance between RIS and MT/MR is larger than the Rayleigh distance of RIS, making far-field assumption applicable and therefore resulting the same performance. As the RIS array dimension increases, the Rayleigh distance of the RIS becomes larger and hence the MT and MR are in the near-field region of the RIS, resulting in different modeling error performance, which is in agreement with the results in Fig. 4. Note that since the Rayleigh distance is a rough approximation of the boundary of far-field and near-field, the modeling error performance of the proposed sub-array partition-based solution will also experience a sudden change when the propagation

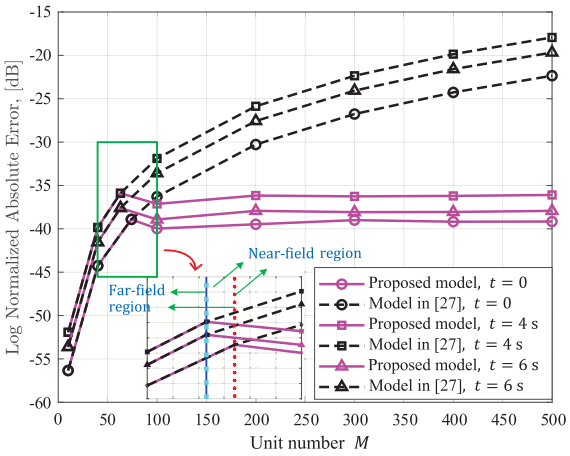

Fig. 5. RIS-assisted V2V channel modeling errors based on the proposed sub-array pattern scheme and conventional method with respect to the motion time of the MT and MR when $v_T = 5$ m/s, $v_R = 5$ m/s, $\eta_T = 0$, and $\eta_R = \pi$.

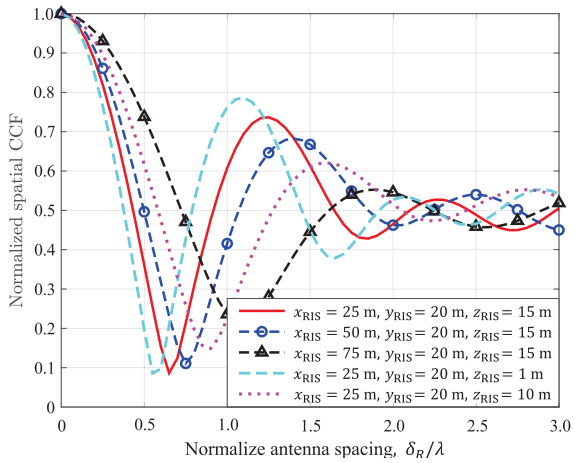

Fig. 6. Spatial CCFs of the proposed channel model based on the proposed sub-array pattern scheme with respect to the RIS location when $t = 2$ s, $K = 1$, $v_T = 5$ m/s, $v_R = 5$ m/s, $\eta_T = 0$, and $\eta_R = 0$.

condition changes from far-field to near-field by increasing the number of units. It is noteworthy to mention that Fig. 5 indicates that the far-field model in [27] show increasing modeling errors as the RIS array dimension increases, whereas the proposed sub-array partition based model retains the nearly constant error performance even with increasing RIS array dimension. This highlights the advantage of the proposed sub-array partition based modeling solution.

C. Spatial CCFs

By utilizing (36), Fig. 6 shows the spatial CCFs of the RIS-assisted V2V channel model based on the proposed sub-array pattern scheme under different RIS locations. It is worth mentioning that (36) is a Bessel function, which leads to fluctuations with the increase of the antenna spacing δ_R/λ; however, the general changing trend of the spatial correlations is to decrease when increasing the antenna spacing. The aforementioned computer simulation results fit the ones in [28] and the measurements in [29] very well, which further validate

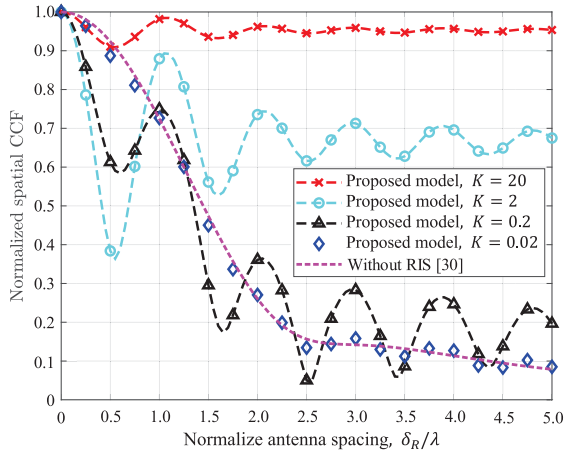

Fig. 7. Spatial CCFs of different propagation links in the proposed channel model with respect to the Rician factor K when $t = 2$ s, $v_T = 5$ m/s, $v_R = 5$ m/s, $\eta_T = 0$, and $\eta_R = \pi$.

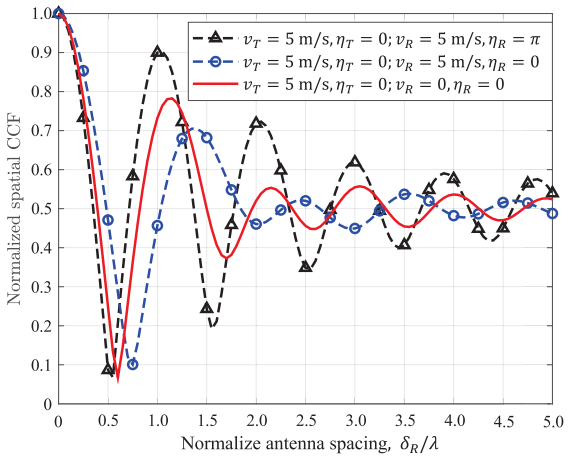

Fig. 8. Spatial CCFs of different propagation links with respect to the motion directions/velocities of the MT and MR when $t = 4$ s and $K = 1$.

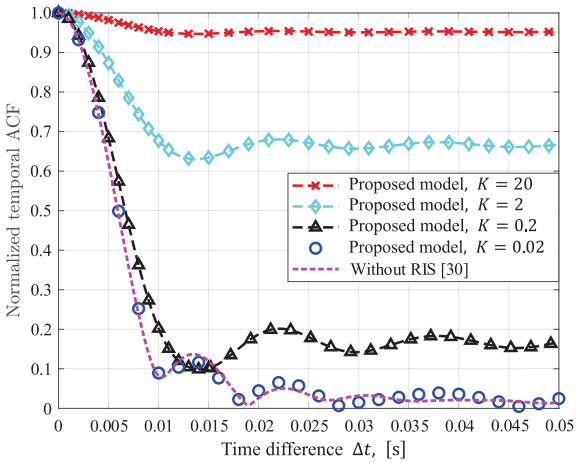

Fig. 9. Temporal ACFs of the proposed channel model with respect to the Rician factor K when $t = 4$ s, $v_T = 5$ m/s, $v_R = 5$ m/s, $\eta_T = 0$, and $\eta_R = 0$.

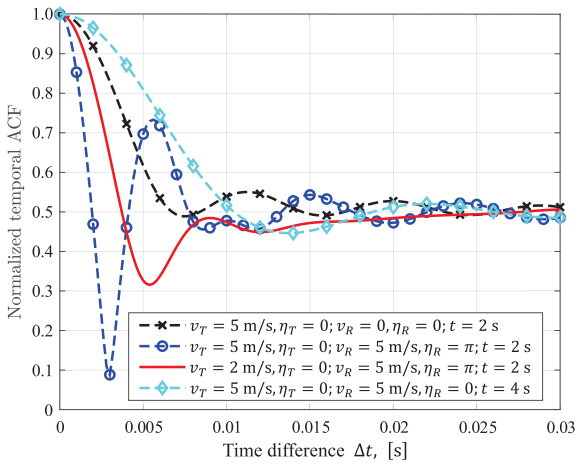

Fig. 10. Temporal ACFs of the proposed channel model with respect to the motion directions/velocities of the MT and MR when $t = 2$ s and $K = 1$.

the accuracy of the derivations and simulation results of the spatial CCFs of the proposed channel model. Another interesting phenomenon is that when we set different locations of the RIS in the proposed channel model, the differences of the behaviors among which are significant.

Fig. 7 shows the spatial CCFs of the proposed channel model under different Rician factors. It can be found that the existence of the RIS links in the proposed channel model lead to the fluctuation of the curves of the spatial correlations. Notice that when the K decreases from 20 to 0.2, the spatial correlations decrease with obviously fluctuations as the normalized antenna spacing δ_R/λ increases. This is different from the curves of the spatial CCFs without RIS [30], which slightly decrease with the increase of the antenna spacing at the MR. Furthermore, we notice that when the Rician factor is very small, i.e., $K = 0.02$, which implies that the energy of the RIS components is negligible as compared with the NLoS components, the spatial correlations show similar decreasing trend as the channel without RIS.

Fig. 8 shows the spatial CCFs of the proposed channel model under different motion properties of the MT and MR. It can be seen that the channel spatial CCF show different descreasing trends under transceiver mobility models. Generally, the spatial CCF decreases faster as the normalized antenna spacing increases when the distance between the MT and MR becomes shorter. It is noteworthy to mention that the spatial CCFs of the proposed channel model firstly fluctuate and then gradually stabilize to a fixed level of $K/(K+1)$ owing to the existence of RIS, which is significantly different from conventional V2V channel model with spatial CCFs smoothly decreasing from unity to zero. This can be interpreted from the fact that the RIS link contributes a deterministic component on the received signals [15].

D. Temporal ACFs

Fig. 9 shows the temporal ACFs of the RIS-assisted V2V channel model based on the proposed sub-array pattern scheme under different Rician factors. It is observed that the correlation properties of the propagation link in time domain gradually decrease as we increase the time difference Δt, which are in agreements with the results in [26] and [30],

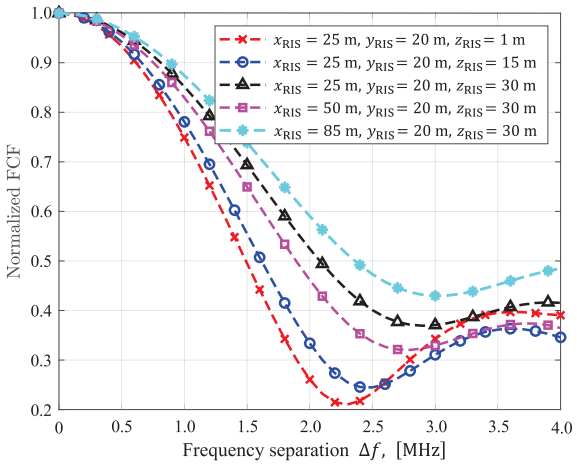

Fig. 11. FCFs of the proposed channel model with respect to the RIS location when $t = 1$ s, $K = 1$, $v_T = 5$ m/s, $\eta_T = 0$, $v_R = 5$ m/s, and $\eta_R = \pi$.

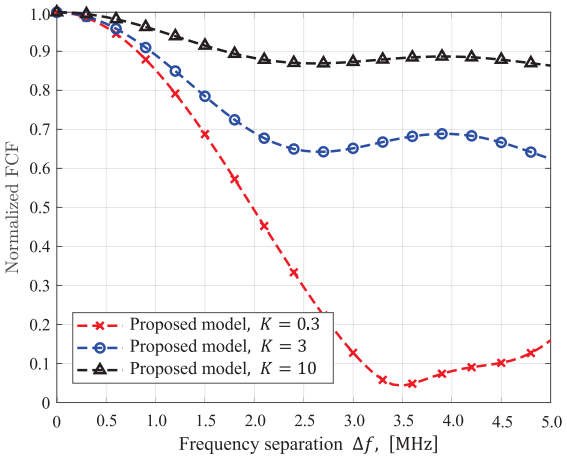

Fig. 12. FCFs of the proposed channel model with respect to the Rician factor when $t = 2$ s, $v_T = 5$ m/s, $\eta_T = 0$, $v_R = 5$ m/s, and $\eta_R = 0$.

thereby demonstrating the accuracy of the derivations and simulation results of the temporal ACFs of the proposed channel model. Furthermore, when we decrease the K from 20 to 0.02, the temporal correlations decrease gradually as the Δt rises from 0 to 0.05 s, which confirm with the observations of the spatial CCFs in Fig. 7.

Fig. 10 shows the temporal ACFs of the proposed channel model under different motion directions/velocities of the MT and MR. It is observed that the temporal correlations behave different characteristics as we set different motion time t. Notice that when we increase the time difference Δt, the fluctuations of the curves of the temporal ACFs decrease gradually. Furthermore, the values of the temporal correlations tend to be stable values $K/(K+1)$ as the Δt keeps increasing, which reason is similar to that in Fig. 8.

E. Frequency Correlation Functions

Fig. 11 indicates that the FCFs of the RIS-assisted V2V channel model based on the proposed sub-array pattern scheme have different values under different RIS locations, which implies the importance of taking into account the RIS locations

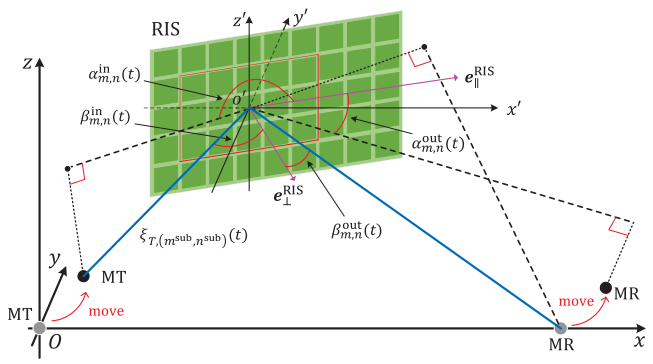

Fig. 13. Illustration of the incident and reflected angles on the RIS. The x'-y'-z' is parallel to the x-y-z and is established by setting the origin o' at the center of the sub-arrays.

in RIS-assisted channel modeling. Furthermore, we notice that the correlation properties of the propagation link in frequency domain gradually decrease as we increase the frequency f, which are in agreements with the results in [30], thereby demonstrating the accuracy of the derivations and simulation results of the FCFs of the proposed channel model.

In Fig. 12, we study the impact of the Rician factor on the channel correlation properties in frequency domain. It shows that when we increase the K from 0.3 to 10, the FCFs increase gradually, which are in agreements with the observations of the spatial CCFs in Fig. 7 and temporal ACFs in Fig. 9, thereby demonstrating the correctness of the aforementioned conclusions.

V. Conclusion

In this paper, we have proposed a sub-array pattern scheme for investigating the RIS-assisted V2V channel propagation characteristics in spatial, time, and frequency domains. It has been demonstrated that the RIS-assisted channel modeling based on the proposed algorithm can achieve the balance between the modeling accuracy and complexity as compared to the conventional methods which are mainly based on the far-field assumption, and thereby showing the superiority of the proposed scheme. Furthermore, based on the sub-array pattern scheme, we have derived and discussed the RIS-assisted V2V channel propagation characteristics, such as spatial CCFs, temporal ACFs, and FCFs. It has been shown that the RIS-assisted V2V channel propagation characteristics are related to the RIS location, as well as the motion time/direction/velocity of the transceivers.

As our future work, we can state three prospective directions: i) conduct measurements for RIS-assisted channel models to further validate the simulation results of the RIS-assisted channel characteristics based on the proposed sub-array pattern scheme; ii) develop more precise approximation algorithms for the boundary of far-field and near-field propagation conditions; iii) derive the path power gains of different propagation links in RIS-assisted channel modeling based on the proposed sub-array partitioning scheme, making the proposed channel model more efficient in describing the overall fading (e.g. large-scale and small-scale fading) characteristics of RIS-assisted communication channels.

$$\Delta\alpha^{\text{in}}_{m,n}(t) = \arccos \frac{\{-\boldsymbol{e}^{\text{RIS}}_{\parallel}\}^{\text{T}} \cdot \{\mathbf{d}_{T,(m^{\text{sub}},n^{\text{sub}})}(t) - \xi_{T,(m^{\text{sub}},n^{\text{sub}})}(t)\cos\beta^{\text{in}}_{m,n}(t)\boldsymbol{e}^{\text{RIS}}_{\perp}\}}{\|-\boldsymbol{e}^{\text{RIS}}_{\parallel}\| \cdot \|\mathbf{d}_{T,(m^{\text{sub}},n^{\text{sub}})}(t) - \xi_{T,(m^{\text{sub}},n^{\text{sub}})}(t)\cos\beta^{\text{in}}_{m,n}(t)\boldsymbol{e}^{\text{RIS}}_{\perp}\|}. \tag{51}$$

$$\begin{aligned}\Delta\alpha^{\text{in}}_{m,n}(t) = \arccos\Bigg\{ & \frac{-\left(d_{T,x}(t) - d_{(m^{\text{sub}},n^{\text{sub}}),x}(t) - \xi_{T,(m^{\text{sub}},n^{\text{sub}})}(t)\cos\beta^{\text{in}}_{m,n}(t)\sin\epsilon_{\text{RIS}}\right)\cos\epsilon_{\text{RIS}}}{\xi_{T,(m^{\text{sub}},n^{\text{sub}})}(t)} \\ & - \frac{\left(d_{T,y}(t) - d_{(m^{\text{sub}},n^{\text{sub}}),y}(t) + \xi_{T,(m^{\text{sub}},n^{\text{sub}})}(t)\cos\beta^{\text{in}}_{m,n}(t)\cos\epsilon_{\text{RIS}}\right)\sin\epsilon_{\text{RIS}}}{\xi_{T,(m^{\text{sub}},n^{\text{sub}})}(t)}\Bigg\}.\end{aligned} \tag{52}$$

$$\alpha^{\text{out}}_{m,n}(t) = 2\pi - \arccos \frac{\{\boldsymbol{e}^{\text{RIS}}_{\parallel}\}^{\text{T}} \cdot \{\mathbf{d}_{R,(m^{\text{sub}},n^{\text{sub}})}(t) - \xi_{R,(m^{\text{sub}},n^{\text{sub}})}(t)\cos\beta^{\text{out}}_{m,n}(t)\boldsymbol{e}^{\text{RIS}}_{\perp}\}}{\|\boldsymbol{e}^{\text{RIS}}_{\parallel}\| \cdot \|\mathbf{d}_{R,(m^{\text{sub}},n^{\text{sub}})}(t) - \xi_{R,(m^{\text{sub}},n^{\text{sub}})}(t)\cos\beta^{\text{out}}_{m,n}(t)\boldsymbol{e}^{\text{RIS}}_{\perp}\|}. \tag{53}$$

$$\begin{aligned}\alpha^{\text{out}}_{m,n}(t) = & 2\pi - \arccos\Bigg\{ \frac{-\left(d_{R,x}(t) - d_{(m^{\text{sub}},n^{\text{sub}}),x}(t) - \xi_{R,(m^{\text{sub}},n^{\text{sub}})}(t)\cos\beta^{\text{out}}_{m,n}(t)\sin\epsilon_{\text{RIS}}\right)\cos\epsilon_{\text{RIS}}}{\xi_{R,(m^{\text{sub}},n^{\text{sub}})}(t)} \\ & - \frac{\left(d_{R,y}(t) - d_{(m^{\text{sub}},n^{\text{sub}}),y}(t) + \xi_{R,(m^{\text{sub}},n^{\text{sub}})}(t)\cos\beta^{\text{out}}_{m,n}(t)\cos\epsilon_{\text{RIS}}\right)\sin\epsilon_{\text{RIS}}}{\xi_{R,(m^{\text{sub}},n^{\text{sub}})}(t)}\Bigg\}.\end{aligned} \tag{54}$$

APPENDIX A

In Fig. 13, we illustrate the time-varying incident and reflected angles on the RIS. Denoting $\boldsymbol{e}^{\text{RIS}}_{\parallel}$ and $\boldsymbol{e}^{\text{RIS}}_{\perp}$ as the directional unit vectors along and perpendicular to the RIS plane, respectively, which can be expressed as

$$\boldsymbol{e}^{\text{RIS}}_{\parallel} = [\cos\epsilon_{\text{RIS}}, \sin\epsilon_{\text{RIS}}, 0]^{\text{T}}, \tag{44}$$

$$\boldsymbol{e}^{\text{RIS}}_{\perp} = [\sin\epsilon_{\text{RIS}}, -\cos\epsilon_{\text{RIS}}, 0]^{\text{T}}. \tag{45}$$

The time-varying distance vectors from the centers of the MT and MR antenna arrays to that of the $(m^{\text{sub}}, n^{\text{sub}})$-th sub-array are respectively expressed as

$$\begin{aligned}\mathbf{d}_{T,(m^{\text{sub}},n^{\text{sub}})}(t) &= \mathbf{d}_T(t) - \mathbf{d}^{\text{origin}}_{m^{\text{sub}},n^{\text{sub}}}(t) \\ &= \begin{bmatrix} d_{T,x}(t) - d_{(m^{\text{sub}},n^{\text{sub}}),x}(t) \\ d_{T,y}(t) - d_{(m^{\text{sub}},n^{\text{sub}}),y}(t) \\ -d_{(m^{\text{sub}},n^{\text{sub}}),z}(t)\end{bmatrix},\end{aligned} \tag{46}$$

$$\begin{aligned}\mathbf{d}_{R,(m^{\text{sub}},n^{\text{sub}})}(t) &= \mathbf{d}_R(t) - \mathbf{d}^{\text{origin}}_{m^{\text{sub}},n^{\text{sub}}}(t) \\ &= \begin{bmatrix} d_{R,x}(t) - d_{(m^{\text{sub}},n^{\text{sub}}),x}(t) \\ d_{R,y}(t) - d_{(m^{\text{sub}},n^{\text{sub}}),y}(t) \\ -d_{(m^{\text{sub}},n^{\text{sub}}),z}(t)\end{bmatrix}.\end{aligned} \tag{47}$$

Therefore, the normal incident angle from the MT to the (m,n)-th unit in the $(m^{\text{sub}}, n^{\text{sub}})$-th sub-array can be expressed as

$$\beta^{\text{in}}_{m,n}(t) = \arccos \frac{\{\boldsymbol{e}^{\text{RIS}}_{\perp}\}^{\text{T}} \cdot \mathbf{d}_{T,(m^{\text{sub}},n^{\text{sub}})}(t)}{\|\boldsymbol{e}^{\text{RIS}}_{\perp}\| \cdot \|\mathbf{d}_{T,(m^{\text{sub}},n^{\text{sub}})}(t)\|}. \tag{48}$$

By substituting (45) and(46) into (48), we can obtain

$$\begin{aligned}\beta^{\text{in}}_{m,n}(t) = \arccos\Bigg\{ & \frac{\left(d_{T,x}(t) - d_{(m^{\text{sub}},n^{\text{sub}}),x}(t)\right)\sin\epsilon_{\text{RIS}}}{\xi_{T,(m^{\text{sub}},n^{\text{sub}})}(t)} \\ & - \frac{\left(d_{T,y}(t) - d_{(m^{\text{sub}},n^{\text{sub}}),y}(t)\right)\cos\epsilon_{\text{RIS}}}{\xi_{T,(m^{\text{sub}},n^{\text{sub}})}(t)}\Bigg\}.\end{aligned} \tag{49}$$

The azimuth angle from the MT to the (m,n)-th unit in the $(m^{\text{sub}}, n^{\text{sub}})$-th sub-array can be expressed as

$$\alpha^{\text{in}}_{m,n}(t) = \begin{cases} \pi - \Delta\alpha^{\text{in}}_{m,n}(t), & \text{if } -d_{(m^{\text{sub}},n^{\text{sub}}),z}(t) > 0 \\ \pi + \Delta\alpha^{\text{in}}_{m,n}(t), & \text{if } -d_{(m^{\text{sub}},n^{\text{sub}}),z}(t) \le 0, \end{cases} \tag{50}$$

with $\Delta\alpha^{\text{in}}_{m,n}(t)$ being expressed as (51), shown at the top of the page. By substituting (44)-(46) into (51), we can rewrite $\Delta\alpha^{\text{in}}_{m,n}(t)$ as (52), shown at the top of the page.

For the RIS link, the azimuth reflected angles from (m,n)-th unit in RIS to MR can be expressed as (53), shown at the top of the page. By substituting (44)-(45) and (47) into (53), we can obtain $\alpha^{\text{out}}_{m,n}(t)$ in (54), shown at the top of the page.

Furthermore, the normal reflected angles from (m,n)-th unit in RIS to MR can be expressed as

$$\beta^{\text{out}}_{m,n}(t) = \arccos \frac{\{\boldsymbol{e}^{\text{RIS}}_{\perp}\}^{\text{T}} \cdot \mathbf{d}_{R,(m^{\text{sub}},n^{\text{sub}})}(t)}{\|\boldsymbol{e}^{\text{RIS}}_{\perp}\| \cdot \|\mathbf{d}_{R,(m^{\text{sub}},n^{\text{sub}})}(t)\|}. \tag{55}$$

By substituting (45) and (47) into (55), we can obtain

$$\begin{aligned}\beta^{\text{out}}_{m,n}(t) = \arccos\Bigg\{ & \frac{\left(d_{R,x}(t) - d_{(m^{\text{sub}},n^{\text{sub}}),x}(t)\right)\sin\epsilon_{\text{RIS}}}{\xi_{R,(m^{\text{sub}},n^{\text{sub}})}(t)} \\ & - \frac{\left(d_{R,y}(t) - d_{(m^{\text{sub}},n^{\text{sub}}),y}(t)\right)\cos\epsilon_{\text{RIS}}}{\xi_{R,(m^{\text{sub}},n^{\text{sub}})}(t)}\Bigg\}.\end{aligned} \tag{56}$$

REFERENCES

[1] I. Yildirim, E. Basar, and I. F. Akyildiz, "Modeling and analysis of reconfigurable intelligent surfaces for indoor and outdoor applications in future wireless networks," *IEEE Trans. Commun.*, vol. 69, no. 2, pp. 1290–1301, Feb. 2021.

[2] E. Basar and I. Yildirim, "Reconfigurable intelligent surfaces for future wireless networks: A channel modeling perspective," *IEEE Wireless Commun.*, vol. 28, no. 3, pp. 108–114, Jun. 2021.

[3] C.-X. Wang, Z. Lv, X. Gao, X. You, Y. Hao, and H. Haas, "Pervasive channel modeling theory and applications to 6G GBSMs for all frequency bands and all scenarios," *IEEE Trans. Veh. Technol.*, vol. 71, no. 9, pp. 9159–9173, Jun. 2022.

[4] H. Jiang, M. Mukherjee, J. Zhou, and J. Lloret, "Channel modeling and characteristics analysis for 6G wireless communications," *IEEE Netw.*, vol. 35, no. 1, pp. 296–303, Jan. 2021.

[5] C.-S. Kim, J.-S. Kim, J.-Y. Hong, J. S. Lim, and Y. J. Chong, "Propagation characteristics of urban and highway vehicle-to-everything (V2X) channels at 5.9 GHz," in *Proc. ICTC*, Jeju Island, (South) Korea, 2021, pp. 872–876.

[6] I. Trindade, F. Muller, and A. Klautau, "Accuracy analysis of the geometrical approximation of MIMO channels using ray-tracing," in *Proc. IEEE LATINCOM*, Santo Domingo, Dominican Republic, 2020, pp. 1–5.

[7] H. Chang et al., "A novel nonstationary 6G UAV-to-ground wireless channel model with 3-D arbitrary trajectory changes," *IEEE Internet Things J.*, vol. 8, no. 12, pp. 9865–9877, Jun. 2021.

[8] B. Xiong, Z. Zhang, J. Zhang, H. Jiang, J. Dang, and L. Wu, "Novel multi-mobility V2X channel model in the presence of randomly moving clusters," *IEEE Trans. Wireless Commun.*, vol. 20, no. 5, pp. 3180–3195, May 2021.

[9] J. Zhang, C. Pan, F. Pei, G. Liu, and X. Cheng, "Three-dimensional fading channel models: A survey of elevation angle research," *IEEE Commun. Mag.*, vol. 52, no. 6, pp. 218–226, Jun. 2014.

[10] H. Jiang, Z. Zhang, L. Wu, J. Dang, and G. Gui, "A 3-D non-stationary wideband geometry-based channel model for MIMO vehicle-to-vehicle communications in tunnel environments," *IEEE Trans. Veh. Technol.*, vol. 68, no. 7, pp. 6257–6271, Jul. 2019.

[11] Y. Yuan, C.-X. Wang, Y. He, M. M. Alwakeel, and E. M. Aggoune, "3D wideband non-stationary geometry-based stochastic models for non-isotropic MIMO vehicle-to-vehicle channels," *IEEE Trans. Wireless Commun.*, vol. 14, no. 12, pp. 6883–6895, Dec. 2015.

[12] J. Huang et al., "Reconfigurable intelligent surfaces: Channel characterization and modeling," *Proc. IEEE*, vol. 110, no. 9, pp. 1290–1311, Jul. 2022.

[13] G. Sun, R. He, Z. Ma, B. Ai, and Z. Zhong, "A 3D geometry-based non-stationary MIMO channel model for RIS-assisted communications," in *Proc. IEEE VTC-Fall*, Norman, OK, USA, Sep. 2021, pp. 1–5.

[14] H. Jiang, R. S. He, C. Ruan, J. Zhou, and D. Chang, "Three-dimensional geometry-based stochastic channel modeling for intelligent reflecting surface-assisted UAV MIMO communications," *IEEE Wireless Commun. Lett.*, vol. 10, no. 12, pp. 2727–2731, Dec. 2021.

[15] B. Xiong, Z. Zhang, H. Jiang, J. Zhang, L. Wu, and J. Dang, "A 3D non-stationary MIMO channel model for reconfigurable intelligent surface auxiliary UAV-to-ground mmWave communications," *IEEE Trans. Wireless Commun.*, vol. 21, no. 7, pp. 5658–5672, Jul. 2022.

[16] B. Xiong et al., "A statistical MIMO channel model for reconfigurable intelligent surface assisted wireless communications," *IEEE Trans. Commun.*, vol. 70, no. 2, pp. 1360–1375, Feb. 2022.

[17] X. Wei, L. Dai, Y. Zhao, G. Yu, and X. Duan, "Codebook design and beam training for extremely large-scale RIS: Far-field or near-field?" *China Commun.*, vol. 19, no. 6, pp. 193–204, Jun. 2022.

[18] P. Mei et al., "On the study of reconfigurable intelligent surfaces in the near-field region," *IEEE Trans. Antennas Propag.*, vol. 70, no. 10, pp. 8718–8728, Feb. 2022.

[19] S. Wu, C. X. Wang, H. Haas, E. H. M. Aggoune, M. M. Alwakeel, and B. Ai, "A non-stationary wideband channel model for massive MIMO communication systems," *IEEE Trans. Wireless Commun.*, vol. 14, no. 3, pp. 1434–1446, Mar. 2015.

[20] H. Jiang, Z. Zhang, J. Dang, and L. Wu, "A novel 3D massive MIMO channel model for vehicle-to-vehicle communication environments," *IEEE Trans. Commun.*, vol. 68, no. 1, pp. 79–90, Jan. 2018.

[21] M. Najafi, V. Jamali, R. Schober, and H. V. Poor, "Physics-based modeling and scalable optimization of large intelligent reflecting surfaces," *IEEE Trans. Commun.*, vol. 69, no. 4, pp. 2673–2691, Apr. 2021.

[22] W. Tang et al., "Wireless communications with reconfigurable intelligent surface: Path loss modeling and experimental measurement," *IEEE Trans. Wireless Commun.*, vol. 20, no. 1, pp. 421–439, Jan. 2021.

[23] W. S. Ellingson, "Path loss in reconfigurable intelligent surface-enabled channels," in *Proc. IEEE PIMRC*, Helsinki, Finland, Sep. 2021, pp. 829–835.

[24] H. Jiang et al., "A general wideband non-stationary stochastic channel model for intelligent reflecting surface-assisted MIMO communications," *IEEE Trans. Wireless Commun.*, vol. 20, no. 8, pp. 5314–5328, Aug. 2021.

[25] Y. Yang, W. Zhang, J. Sun, and C. X. Wang, "A 3D wideband non-stationary GBSM for RIS-assisted communications in outdoor scenarios," in *Proc. IEEE ICECE*, Xi'an, China, Dec. 2021, pp. 210–214.

[26] C. F. López and C.-X. Wang, "Novel 3-D non-stationary wideband models for massive MIMO channels," *IEEE Trans. Wireless Commun.*, vol. 17, no. 5, pp. 2893–2905, May 2018.

[27] Y. Sun, C.-X. Wang, J. Huang, and J. Wang, "A 3D non-stationary channel model for 6G wireless systems employing intelligent reflecting surfaces with practical phase shifts," *IEEE Trans. Cogn. Commun. Netw.*, vol. 7, no. 2, pp. 496–510, Jun. 2021.

[28] G. Sun et al., "A 3D wideband channel model for RIS-assisted MIMO communications," *IEEE Trans. Veh. Technol.*, vol. 71, no. 8, pp. 8016–8029, Aug. 2022.

[29] S. Payami and F. Tufvesson, "Channel measurements and analysis for very large array systems at 2.6 GHz," in *Proc. 6th Eur. Conf. Antennas Propag. (EUCAP)*, Prague, Czech Republic, Mar. 2012, pp. 433–437.

[30] J. Bian, C.-X. Wang, X. Q. Gao, X. You, and M. Zhang, "A general 3D non-stationary wireless channel model for 5G and beyond," *IEEE Trans. Wireless Commun.*, vol. 20, no. 5, pp. 3211–3224, May 2021.

Hao Jiang (Member, IEEE) received the B.S. and M.S. degrees in electrical and information engineering from the Nanjing University of Information Science and Technology, Nanjing, China, in 2012 and 2015, respectively, and the Ph.D. degree from Southeast University, Nanjing, in 2019. From 2017 to 2018, he was a visiting student with the Department of Electrical Engineering, Columbia University, New York, NY, USA. He is currently an Associate Professor with the Artificial Intelligence/School of Future Technology, Nanjing University of Information Science and Technology. His current research interests include the general area of wireless channel measurements and modeling, 6G wireless communication networks, signal processing, machine learning, and AI-driven technologies.

Baiping Xiong received the B.Eng. degree in information engineering from Southeast University, Nanjing, China, in 2019, where he is currently pursuing the Ph.D. degree with the National Mobile Communications Research Laboratory.

Hongming Zhang (Member, IEEE) received the B.Eng. degree (Hons.) in telecommunications from the Nanjing University of Aeronautics and Astronautics (NUAA) and the City University of London, in 2011, and the M.Sc. and Ph.D. degrees in wireless communications from the University of Southampton in 2012 and 2017, respectively. From 2017 to 2018, he was with the Department of Electrical Engineering, Columbia University, New York, NY, USA. He is currently an Associate Professor with the School of Information and Communication Engineering, Beijing University of Posts and Telecommunications, Beijing, China. His research interests include wireless communications, heterogeneous network performance analysis and optimization, and machine learning.

Ertugrul Basar (Fellow, IEEE) received the Ph.D. degree from Istanbul Technical University in 2013. He is currently an Associate Professor with the Department of Electrical and Electronics Engineering, Koc University, Istanbul, Turkey and the Director of the Communications Research and Innovation Laboratory (CoreLab). He was a Mercator Fellow with Ruhr University Bochum, Germany, in 2022, and a Visiting Research Collaborator with Princeton University, USA, from 2011 to 2012. His primary research interests include beyond 5G and 6G wireless networks, communication theory and systems, reconfigurable intelligent surfaces, index modulation, waveform design, and signal processing for communications. He is a young member of the Turkish Academy of Sciences in 2017. He served as the Editor/Senior Editor for many journals, including IEEE COMMUNICATIONS LETTERS from 2016 to 2022, IEEE TRANSACTIONS ON COMMUNICATIONS from 2018 to 2022, *Physical Communication* from 2017 to 2020, and IEEE ACCESS from 2016 to 2018. Currently, he is the Editor of *Communications and Networks* (Frontiers).